ScienceDirect

International Journal of Hydrogen Energy

Volume 189, 17 November 2025, 152115

Accelerated numerical simulations of hydrogen flames: Open-source implementation of an advanced diffusion model library in OpenFOAM

Ali Haider [a 1], Ilya Morev [a 1], Aleksi Rintanen [a 1], Zin Shahin [a 1], Parsa Tamadonfar [a], Shervin Karimkashi [a], Armin Wehrfritz [b], Ville Vuorinen [a]

Show more

Outline | Share Cite

https://doi.org/10.1016/j.ijhydene.2025.152115

Get rights and content

Highlights

- Numerically stable, open-source implementation of two diffusion models featuring velocity correction.
- Functionality and robustness are demonstrated for various test cases including 3D hydrogen burners.
- The newly developed FickianTransportFoam library is made openly available.
- Significant computational efficiency improvement is demonstrated using DLBFoam and FickianTransportFoam for hydrogen flames.

Abstract

Here, the OpenFOAM software with the dynamic load balancer library DLBFoam is investigated for computational fluid dynamics (CFD) simulations of different hydrogen (H_2) flames. The benefits of DLBFoam for hydrogen have not been thoroughly investigated in the past. To explore this, a new open-source diffusion model library FickianTransportFoam is implemented in this study. FickianTransportFoam includes species-specific constant Lewis number and mixture-averaged models with correction velocity to account for preferential diffusion. The model is first verified for one-dimensional (1D) premixed and non-premixed counterflow flames. Additionally, four hydrogen/air flames are explored: (1) two-dimensional (2D) laminar freely propagating premixed flame, (2) 2D axisymmetric laminar non-premixed jet flame, (3) three-dimensional (3D) turbulent non-premixed swirling flame, and (4) 3D turbulent premixed swirling flame. The

main results and achievements regarding the implemented transport models are as follows. First, the results from 2D freely propagating flame demonstrated thermodiffusively unstable flame formation using the mixture averaged model. The analytical and numerical dispersion relationships agree well for the linear instability growth phase. Second, the model functionality is demonstrated for a laminar 2D jet case with conjugate heat transfer. Furthermore, validation and grid sensitivity studies for the 3D turbulent flames are carried out. Third, the computational benchmark for each configuration indicates a factor of ∼10-100 speed-up when utilizing DLBFoam. Finally, the test cases and source codes for FickianTransportFoam are openly shared.

Graphical abstract

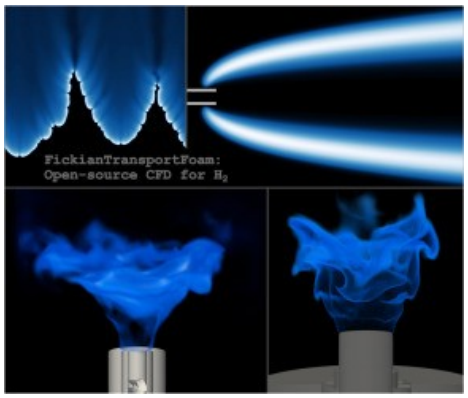

Download: Download high-res image (203KB)

Download: Download full-size image

Previous Next

Keywords

High-performance computing; Unstructured meshes; Hydrogen flames; DLBFoam; OpenFOAM; Diffusion transport model

1. Introduction

Hydrogen is considered to be one of the key clean energy carriers that could potentially contribute to reducing greenhouse gas emissions and air pollutants [1]. However, despite its benefits, hydrogen utilization presents several technological challenges due to, e.g. its high laminar burning velocity, high mass diffusivities, and low volumetric energy density [2], [3]. For instance, the high mass diffusivities of molecular and atomic hydrogen may lead to anomalous phenomena such as thermodiffusive instabilities under lean conditions [4]. This phenomenon may lead to a more pronounced flashback in combustion devices due to the highly increased fuel consumption speeds compared to the unstretched laminar burning velocity [5]. It should be noted that computational fluid dynamics (CFD) is one of the key present-day tools to design combustion devices. However, scale-resolving simulations of chemically reactive flows are computationally expensive and many challenges are usually encountered in order to model such flames [6]. In particular, special effort needs to be made on transport modeling to accurately capture differential diffusion and thermodiffusive effects in hydrogen flames, which originate from the disparity of mass and thermal diffusivities and therefore cannot be modeled accurately using a common unity Lewis number assumption [7]. As shown in recent studies, such microscale effects can be important also in turbulent hydrogen/air flames [8], [9]. Hence, one of the core objectives of this

paper is to present an open-source transport model library, `FickianTransportFoam` which is benchmarked in laminar and turbulent flow cases using large-eddy simulation (LES).

CFD code development and validation for numerical simulations of reactive flows requires gathering high-quality experimental and computational data. For example, since 1996, the TNF workshop [10] has aimed to collect detailed flame data in well-defined configurations to improve the understanding of turbulent combustion. With growing interests in hydrogen combustion, in May 2023, three experimental datasets for hydrogen flames were made available on the TNF workshop website via the Clean Aviation working group initiative [11]. The three flame configurations are the Toulouse rig (Hydrogen Low NOx burner, HYLON), the TU Berlin rig (Advanced Hybrid Engines for Aircraft Development project burner, AHEAD), and the NTNU rig (bluff body stabilized burner). The main objective of this initiative is to verify and validate different CFD codes against accurate experimental measurements, such as particle image velocimetry (PIV) and chemiluminescence imaging. Various experimental studies have already been conducted on these test rigs. For instance, Aniello et al. and Marragou et al. [12], [13] conducted an experimental study on the HYLON setup investigating the stabilization mechanisms of non-premixed and partially premixed hydrogen/air swirl-stabilized flames. Reichel et al. [14], [15], [16] investigated a swirling hydrogen flame in the AHEAD setup and studied the impact of axial air injection on lean premixed hydrogen flames. Æsøy et al. [17] conducted a thorough investigation on the bluff body stabilized premixed flame (NTNU rig). The studies cover various flame characteristics including flame-flame interactions, acoustic response, and suppression of thermoacoustic instabilities under different conditions. As part of the present study, the reactive flows of H_2 in HYLON and AHEAD setups are chosen for validation and investigation.

In addition to experimental data on hydrogen flames, there has been growing interest in numerical investigations of both premixed and diffusion hydrogen flames during the past decade. In the context of premixed flames, Berger et al. [5] conducted detailed numerical simulations of intrinsic combustion instabilities in two-dimensional (2D) freely propagating premixed hydrogen mixtures. The species diffusivities were determined by the species-specific constant Lewis number approach. To ensure mass conservation, the velocity-correction method was applied to the species diffusion velocity. The study investigated the tendency of the premixed hydrogen flames to develop intrinsic instabilities under various conditions. These instabilities become stronger with increasing (decreasing) pressure (equivalence ratio and unburned temperature). In a follow-up paper, Berger et al. [4] discussed the long-term dynamics of these flames in larger computational domains, observing significant flame front wrinkling and variations in local reaction rates and flame thickness. Mira et al. [18] investigated lean premixed hydrogen flames in the AHEAD setup, validating a large-eddy simulation (LES) framework with the flamelet model relying on the presumed-shape probability density function approach. They employed the Alya code [19] with the unity Lewis assumption for the species mass diffusivity in order to simplify the transport model. The study emphasized the importance of the axial momentum ratio for flame stabilization and density stratification for suppressing instabilities at the flashback onset. Furthermore, Capurso et al. [20] validated the AHEAD configuration using the AVBP code [21] by employing LES with NOx analysis. The dynamic thickened flame model [22] was used and coupled with the species-specific constant Lewis number transport modeling approach. It was shown that the numerical configuration used in the study, along with the reduced skeletal scheme, can accurately capture the level of NOx emissions in lean hydrogen flames.

In the context of non-premixed flames, Cheng et al. [23] analyzed experimental and numerical laminar hydrogen jet non-premixed flames to understand the influence of thermal diffusion (Soret effect), different chemical kinetic mechanisms, and boundary conditions on the flame structure using the CFD-ACE software. The importance of conjugate heat transfer (CHT) and thermal diffusion was demonstrated. Additionally, Aniello et al. [12] conducted experimental and numerical studies on the HYLON setup based on two different stabilized flame scenarios: first, a flame anchored to the injector's lip forming an M-shaped flame (Flame A), and second, an aerodynamically stabilized V-shaped lifted flame (Flame L). LES was performed using the AVBP code, with the same combustion and transport models as described in [20]. It was observed that the anchored flame burns

fully in a non-premixed (diffusion controlled) mode, while the lifted flame possesses the characteristics of both premixed and non-premixed modes, i.e. a partially premixed flame.

In order to respond to the current high demand in the development and validation of open-source CFD codes for hydrogen reactive flows, this study extends and validates the recently developed `DLBFoam` library for hydrogen flame simulations. `DLBFoam` is an open-source library to accelerate the computation of reactive flows. It was initially developed by Kahila et al. [24], [25], and extended in works by Tekgül et al. [26] and Morev et al. [27], who also tested this library for fossil fuel flames with relatively large chemical kinetic mechanisms. The integration of `DLBFoam` functionality to other tools such as `DetonationFoam` [28], `DeepFlame` [29], and `ARCFoam` [30], by our and other research groups around the world, indicates its potential for accelerating reactive flow simulations. This library has been used in a wide range of advanced reactive flow simulations for both fundamental and industrial applications [31], [32], [33], [34], [35], [36], [37], [38].

Most of the CFD codes currently used to simulate hydrogen flames with preferential diffusion (e.g. AVBP [21], CFD-ACE [39], and Alya [19]) are either in-house or commercial codes. As an exception, Dasgupta et al. [40] published an open-source solver for `OpenFOAM` with advanced diffusion models for direct numerical simulations DNS or implicit LES (ILES). The test cases included laminar and turbulent simulations in fundamental test cases, including non-premixed jet flames and shear layers. Another notable example is the `reactingDNS` code, with an implementation of mixture-averaged diffusion model for DNS [41], [42], [43], [44], [45]. In the present study, we present an open-source code compatible with LES turbulence modeling and several test cases on different combustion modes, including premixed and non-premixed turbulent combustion in 3D complex geometries.

Based on the presented literature survey, the following research gaps are identified. First, accurate open-source diffusion models compatible with a dynamic load balancer and LES are scarce in the literature. This is particularly true in the context of the `OpenFOAM` code. Second, the benefits of `DLBFoam` for pure hydrogen test cases (with significantly smaller chemical kinetic mechanisms compared to the previously published test cases) in both fundamental and industrial applications have not been previously explored.

With respect to the above-mentioned challenges and requirements for the development and testing of accurate and cost-effective CFD codes for hydrogen flames, the present paper introduces the following novel contributions. First, the paper develops and offers an open-source library of transport models, `FickianTransportFoam` [46], which includes a numerically stable implementation of the species-specific constant Lewis number model and the mixture-averaged transport model using the velocity-correction approach, both of which are not available in the most recent version of `OpenFOAM` (version 12). Additionally, the paper presents the computational efficiency of using the `DLBFoam` and the `FickianTransportFoam` libraries by conducting a validation and benchmark study of four distinct pure hydrogen flames, with all the setups made openly available, including meshes, solver settings, discretization schemes, initial and boundary conditions, as well as instructions to run the cases [47].

2. Methodology

2.1. Overview of the numerical approach

Similar to our earlier studies [24], [25], [26], [27], the governing equations of reactive flows include the complete Navier–Stokes equations for density, momentum, and sensible enthalpy along with the species transport equations. The baseline flow solver to solve these equations is `reactingFoam` from the finite volume method (FVM) framework in `OpenFOAM-v10` [48]. `reactingFoam` enforces mass conservation by solving transport equations only for $N_s - 1$ species and calculating the mass fraction of the last specie as $Y_{N_s} = 1 - \sum_{k=1}^{N_s-1} Y_k$. Chemistry is modeled using the chemical kinetic mechanism of Capurso et al. [20]. The governing equations are discretized with the second-order backward scheme in time and the convection terms are discretized with a second-order limited linear scheme, if not stated otherwise. The details of the settings

are openly shared along with the tutorial cases. Operator splitting is used to decouple the chemical source terms from the species and sensible enthalpy transport equations. The PIMPLE algorithm [49] is used to couple the flow equations. The different stages of the algorithm in the `reactingFoam` solver are visualized in Fig. 1 with external plugins highlighted.

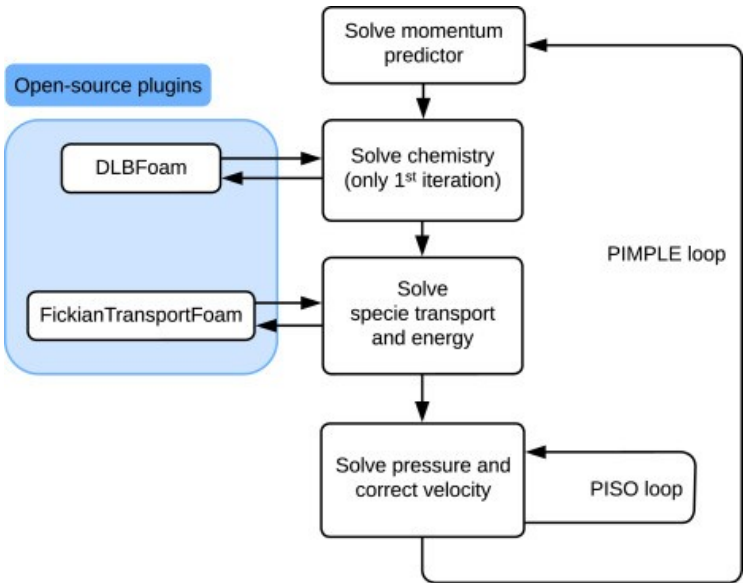

Download: Download high-res image (249KB)

Download: Download full-size image

Fig. 1. A schematic showing the main steps of the `reactingFoam` solver within a single CFD time step with `DLBFoam` and `FickianTransportFoam` plugins.

`DLBFoam` has been discussed in detail in our previous publications [26], [27]. Next, we briefly outline the main features of `DLBFoam`. The purpose of `DLBFoam` is to optimize the chemistry solution procedure on two levels: domain-level dynamic chemistry solution load balancing between the processors and cell-level improvement of the integration process. As operator splitting is applied for chemistry source terms, the chemistry ODE system of a particular cell becomes dependent only on the local conditions in the cell before integration. This makes the chemistry problem easily transferrable between computational processors, enabling load balancing. The need for balancing arises from widely different mixture conditions across the computational domain, leading to differences in local stiffness of a chemical ODE system integration problem, and, in turn, to different solution times. In `DLBFoam`, load balancing is done dynamically: the chemistry load imbalance is evaluated on a given time step, and chemistry problems for the next time step are assigned between the processors accordingly. At the cell level, the computational efficiency of each integration is improved using the analytical Jacobian formulation of pyJac [50] and LU-decomposition together with back-substitution routines from LAPACK [51]. Additionally, the `Seulex` solver implementation follows the original Fortran implementation [52]. Furthermore, a reference mapper feature is used for non-premixed cases. The purpose of this feature is to identify large groups of cells with similar chemistry outside the main reaction zones (mixture fraction $Z < Z_{max}$, temperature $T < T_{ambient} + \Delta T_{max}$).

As shown in our previous studies, the `DLBFoam` library may offer significant speed-up (up to 2–3 orders of magnitude for hydrocarbons) over the previous reactive flow solvers in `OpenFOAM` (versions 7 and 8) [26], [27]. In the context of hydrogen combustion, the chemical kinetic mechanisms are relatively small. For example, throughout the present study, we utilize themechanism of Capurso et al. [20] with only **15** species. For such small mechanisms, the improvement brought by the cell-level optimization might be relatively small. However, in complex geometries, especially where upstream regions are modeled (e.g. mixing chambers, swirlers), the benefit of the load-balancing might be significant due to the large amount of processors with mostly non-stiff chemistry problems (i.e. non-reactive flow parts), requiring low computational effort. In fact, the chemical

mechanism proposed by Capurso et al. [20], has been previously used in LES simulations in the context of the AHEAD burner, which is also among the test cases studied herein.

More information on the numerical approach can be found in the openly published case setups [47]. Since hydrogen requires special treatment of the molecular transport, the `FickianTransportFoam` library is introduced and discussed next.

2.2. Implemented transport models

High mass diffusivity of molecular and atomic hydrogen requires particular modeling attention to the corresponding terms in the equations. The unfiltered transport equations for species mass fraction Y_k and sensible enthalpy h_s are written as follows:

$$\frac{\partial}{\partial t}(\rho Y_k) + \nabla\cdot(\rho \mathbf{u} Y_k) = -\nabla\cdot\mathbf{j}_k + \dot{\omega}_k \tag{1}$$

and

$$\frac{\partial}{\partial t}(\rho h_s) + \nabla\cdot(\rho \mathbf{u} h_s) + \frac{\partial}{\partial t}(\rho K) + \nabla\cdot(\rho \mathbf{u} K) = \frac{\partial p}{\partial t} - \nabla\cdot\mathbf{q} + \dot{\omega}_T, \tag{2}$$

where $\dot{\omega}_k, \dot{\omega}_T$, and K denote the reaction source term for specie k, heat release rate, and kinetic energy, respectively. In the `reactingFoam` solver, the kinetic energy containing terms are evaluated explicitly while Eq. (2) is solved for the sensible enthalpy. The mass flux $\mathbf{j}_k$ of species k is written in terms of the diffusion velocity $\mathbf{V}_k$

$$\mathbf{j}_k = \rho Y_k \mathbf{V}_k \tag{3}$$

and the heat flux $\mathbf{q}$ assuming Fourier's law

$$\mathbf{q} = -\lambda\nabla T + \sum_{k=1}^{N} h_{s,k}\mathbf{j}_k, \tag{4}$$

where λ is the mixture thermal conductivity and $h_{s,k}$ is the sensible enthalpy of specie k. In `FickianTransportFoam`, two different mathematical forms are available for discretizing the Fourier's heat flux term $-\lambda\nabla T$. In the first form, the heat flux is expressed in terms of the solution variable h_s using the relation $dh_{s,k} = c_{p,k}\,dT$ yielding

$$-\lambda\nabla T = -\frac{\lambda}{c_p}\nabla h_s + \frac{\lambda}{c_p}\sum_{k=1}^{N} h_{s,k}\nabla Y_k, \tag{5}$$

which allows implicit treatment of the first term on the right-hand side, and is used in cases 1, 3 and 4. However, to maintain compatibility with the default `OpenFOAM` boundary conditions for CHT, the original `OpenFOAM` formulation is retained using the explicit temperature gradient with an implicit correction term for case 2 [53].

The expression for the ordinary diffusion velocity is obtained following Kee et al. [54] as

$$\mathbf{V}'_k = -\frac{D_k}{Y_k}\nabla Y_k, \tag{6}$$

where D_k denotes a model-specific diffusion coefficient. To enforce mass conservation, a velocity-correction approach is used, where a correction velocity $\mathbf{V_c}$ is introduced as

$$\begin{aligned}\mathbf{V}_k &= \mathbf{V}'_k + \mathbf{V_c},\\ \mathbf{V_c} &= -\sum_{k=1}^{N} Y_k \mathbf{V}'_k.\end{aligned} \tag{7}$$

In the present work, two different transport models for diffusion coefficients are implemented: (1) the mixture-averaged and (2) the species-specific constant Lewis number models. In the mixture-averaged approach, the model diffusion coefficients are evaluated from the binary diffusion coefficients $\mathscr{D}_{jk}$. The

mixture-averaged diffusion coefficients in Eq. (6) can be derived from the Stefan–Maxwell equation, invoking the Hirschfelder–Curtiss approximation [55], and subsequently read

$$D_k = \left(\sum_{j\neq k} \frac{X_j}{\mathscr{D}_{jk}} + \frac{X_k}{1-Y_k}\sum_{j\neq k}\frac{Y_j}{\mathscr{D}_{jk}}\right)^{-1}, \tag{8}$$

where X_j is the molar fraction of specie j [54]. The binary diffusion coefficients are evaluated from polynomial expressions of temperature, inversely proportional to pressure, i.e. $\mathscr{D}_{jk} = \mathscr{D}_{jk}(T, p)$, which are calculated in `Cantera` based on the kinetic theory of gases [56].

Here, the mixture-averaged transport model is employed for the one- and two-dimensional reactive flow cases as well as for the three-dimensional non-premixed case. For the premixed turbulent three-dimensional case, a simpler diffusion model based on species-specific constant Lewis number (Le_k) is adopted to demonstrate the validity of the implemented model also in the species-specific constant Lewis number approach. Such an approach has been investigated in several hydrogen-specific applications in the past [4], [20], [57], [58], [59], [60] and hence it is also implemented as part of `FickianTransportFoam`. Details regarding the calculation of species-specific Lewis numbers and the values used in the present simulations are provided in the Supplementary Data file Section S1.4. In the species-specific constant Lewis number approach, the diffusion coefficients are obtained from the thermal diffusivity α of the gas mixture as $D_k = \alpha/Le_k$. As a remark, we note that the presented diffusion models are also compatible with the explicit large-eddy simulation (LES) subgrid scale models.

Although an implementation of the mixture-averaged transport model `FickianFourier` is available in `OpenFOAM` (since version 9), we note that it does not include the correction velocity $\mathbf{V_c}$. It is known that such an assumption may lead to unstable behavior when the mixture is not greatly diluted by the last specie. Furthermore, `OpenFOAM` (versions 9–12) implements the mixture-averaged diffusion coefficient D_k expression differently than in Eq. (8). The form used in OpenFOAM is more suitable if diffusion velocity $\mathbf{V}'_k$ in Eq. (6) is expressed in terms of mole fraction gradients rather than in terms of mass fraction gradients [54]. The newly implemented code includes the correct formulation (see Eq. (8)) and handles the limiting cases of the pure species ($Y_k \to 1$) in a robust manner by switching from the mixture-averaged coefficient D_k to the self-diffusion coefficient $\mathscr{D}_{kk}$ at a user-defined mass fraction limit. The mass conservation properties of the new implementation and the native model are demonstrated in the Supplementary Data file Section S1.1.

2.3. Turbulence and combustion models

The LES employs the WALE subgrid-scale model [61]. The WALE model has been widely used to predict complex turbulence phenomena in gas turbine combustors [57], [58], [62], [63]. Hence, the WALE model is also used for the 3D test cases studied herein. In the WALE model, the subgrid viscosity is given as

$$\nu_t = (C_w \Delta)^2 \frac{\left(\mathscr{S}^d_{ij}\mathscr{S}^d_{ij}\right)^{3/2}}{\left(\tilde{S}_{ij}\tilde{S}_{ij}\right)^{5/2} + \left(\mathscr{S}^d_{ij}\mathscr{S}^d_{ij}\right)^{5/4}}, \tag{9}$$

where the strain rate tensor is defined $\tilde{S}_{ij} = \frac{1}{2}(\partial\tilde{u}_i/\partial x_j + \partial\tilde{u}_j/\partial x_i)$, model constant $C_w = 0.325$, Δ is the filter width and

$$\mathscr{S}^d_{ij} = \frac{1}{2}\left(\frac{\partial\tilde{u}_i}{\partial x_k}\frac{\partial\tilde{u}_k}{\partial x_j} + \frac{\partial\tilde{u}_j}{\partial x_k}\frac{\partial\tilde{u}_k}{\partial x_i}\right) + \frac{1}{3}\frac{\partial\tilde{u}_k}{\partial x_m}\frac{\partial\tilde{u}_m}{\partial x_k}\delta_{ij}. \tag{10}$$

In the present work, we investigate four test cases 1–4 introduced in the following section. For cases 1–3, the 'no turbulence-chemistry interaction (TCI)' i.e. the perfectly stirred reactor (PSR) model is adopted. For case 4 (3D premixed), the partially stirred reactor (PaSR) [64] combustion modeling approach is adopted in which the species reaction rates are scaled using a segregation factor κ ($0 \leq \kappa \leq 1$) to distinguish between the reacting and non-reacting fractions inside a computational cell. The filtered species reaction rate from Eq. (1) is calculated as,

$$\overline{\dot{\omega}_k(Y,T)} = \kappa\,\dot{\omega}_k\left(\widetilde{Y_k},\widetilde{T}\right) \tag{11}$$

where $\dot{\omega}_k$ is obtained from solving system of ordinary differential equations based on the Arrhenius equations using resolved species mass fractions and temperature. The segregation factor κ is defined based on the chemical (τ_c) and mixing (τ_{mix}) time scales, as follows,

$$\kappa = \frac{\tau_c}{\tau_c+\tau_{mix}}, \tag{12}$$

The chemical time scale is defined as

$$\tau_c = \frac{\sum_{r=1}^{N_{reactions}}(w_{f,r}+w_{r,r})}{\sum_{r=1}^{N_{reactions}}\left(w_{f,r}^2+w_{r,r}^2\right)}\,c_{tot}, \tag{13}$$

where $c_{tot} = \sum_i c_i$ is the total molar concentration, and the forward and reverse molar production contributions for reaction r are defined as

$$w_{f,r} = \dot{\omega}_{f,r}\sum_{i\in products}\nu_{r,i}, \tag{14}$$

$$w_{r,r} = \dot{\omega}_{b,r}\sum_{i\in reactants}\nu_{r,i}, \tag{15}$$

Here, $\dot{\omega}_{f,r}$ and $\dot{\omega}_{b,r}$ are the forward and backward molar reaction rates per unit volume, respectively, and $\nu_{r,i}$ are the stoichiometric coefficients of the participating species. The mixing time scale (Kolmogorov time scale), τ_{mix} [65], is expressed as,

$$\tau_{mix} = C_{mix}\sqrt{\frac{\nu_{eff}}{\epsilon}}, \tag{16}$$

where $\nu_{eff} = \nu + \nu_t$ is the effective viscosity (sum of molecular viscosity ν and turbulent viscosity ν_t) and ϵ is the dissipation rate. C_{mix} is a constant used to limit the mixing time scale. In the present study, C_{mix} is set to 1.

2.4. Numerical setups

The four different hydrogen flame cases that are studied in this work are represented in Fig. 2. The first two cases are laminar flames under (a) premixed and (b) non-premixed conditions. The two latter cases are turbulent swirl-stabilized flames in (c) non-premixed and (d) premixed conditions. The numerical details of each case setup are provided in Table 1. Each of the cases is discussed in more detail below.

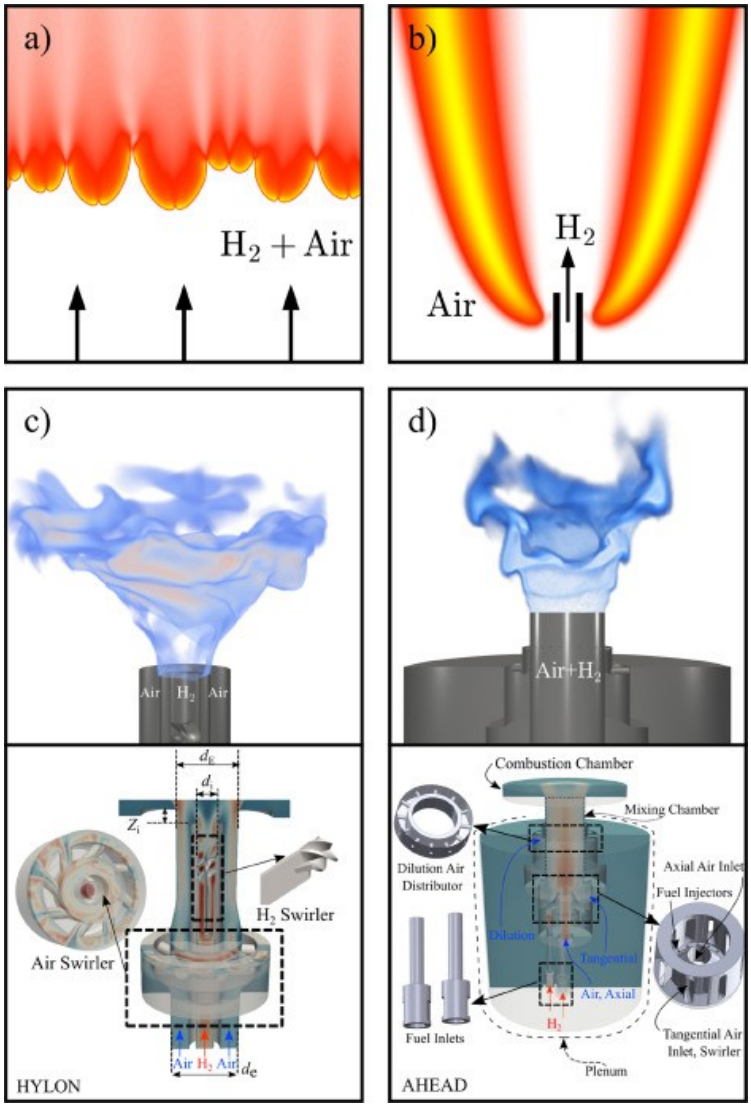

Download: Download high-res image (773KB)

Download: Download full-size image

Fig. 2. Schematic pictures of the numerical hydrogen flame configurations. (a) 2D laminar freely propagating premixed planar flame, (b) 2D axisymmetric laminar non-premixed jet flame, (c) 3D turbulent non-premixed flame (HYLON, Flame A), and (d) 3D turbulent premixed flame (AHEAD).

Table 1. Summary of the studied configurations.

Case	Premixed (2D)	Non-premixed (2D)	HYLON (3D)	AHEAD (3D)
Modeling approach	DNS	DNS	LES/WALE	LES/WALE
Diffusion model	Mixture-avg.	Mixture-avg.	Mixture-avg.	$\boldsymbol{Le_k = \text{const.}}$
Mesh size	4M	0.25M	24M	64.9M

2.4.1. Case 1: 2D laminar freely propagating premixed flame

First, a 2D laminar freely propagating premixed flame is studied. Based on the previous works in the literature, such a case is expected to represent the thermodiffusively unstable characteristic of lean hydrogen flames [4]. Two different simulation sets are carried out to investigate: (1) dispersion analysis, where the linear growth phase is studied with varying flame front perturbation wavelength (at equivalence ratios $\boldsymbol{\phi = 0.5/1.0/1.5}$), and (2) the long-term large-scale flame dynamics (at $\boldsymbol{\phi = 0.5}$).

Fig. 2a represents the numerical domain, where the flame propagates downwards against the fuel-oxidizer stream. The domain width for the dispersion analysis is chosen based on the investigated wavelength and the height of the domain is 20 laminar flame thicknesses δ_L^0, calculated as $\delta_L^0 = \frac{T_b - T_u}{\max(\nabla T)}$ (subscript b stands for burnt, subscript u stands for unburnt). Regarding the large-scale simulation, the domain size is 200 × 200 δ_L^0. The computational grid is made fine enough so that the cell size is $\Delta x = \Delta y = \delta_L^0/10$, for the large domain (while $\delta_L^0/20$ is used for the small domains). The time step is set to a fixed value, so that the thermal diffusivity based maximum CFL number is 0.3. Periodic boundary conditions are imposed in the lateral direction. At the inflow boundary, hydrogen and air mass fractions are set to a constant value while at the exit, zero-gradient boundary condition is set for all species. For the large-scale simulation, the velocity of the mixture at the input is set to an estimate of the consumption speed and is adjusted manually over the course of the simulation to keep the flame front away from the boundaries. For the dispersion analysis, the inlet velocity is fixed equal to the respective laminar burning velocity S_L^0. The wave-transmissive boundary condition is applied to the pressure inlet and outlet to avoid any pressure wave reflections at the boundaries. The domain is initialized with a steady-state solution of a 1D freely propagating flame with a small spatial sinusoidal perturbation introduced in the flame front. The convection terms are discretized with a third-order limited cubic scheme. It should be noted that `Cantera` is used to evaluate the required flame and mixture properties (e.g. laminar burning velocity and Prandtl number) in the analytical dispersion relations.

2.4.2. Case 2: 2D axisymmetric laminar non-premixed jet flame

Second, the 2D axisymmetric laminar non-premixed flame is studied. Fig. 2b shows the schematic of the numerical configuration of the laminar jet flame at $Re = 330$, investigated experimentally and numerically by Cheng et al. [23]. Hydrogen is injected through a vertical steel pipe with an inner diameter of 1 mm and a wall thickness of 0.17 mm into the ambient air (101 kPa, 300 K). In the experiment, the temperatures, concentrations of the major species (O_2, N_2, H_2O, H_2) and hydroxyl radical (OH) are measured in multiple spatial locations.

In the numerical setup, a two-dimensional wedge-type mesh is used. The size of the computational domain is 150 mm × 30 mm, which is assumed to be large enough to minimize the effect of the boundary conditions on the flame, based on earlier test simulations with a substantially larger domain size. A close-up view of the mesh at the exit of the nozzle and in the flame region is shown in Fig. 3a. The resolved height of the nozzle within the domain is 30 mm, where both heat transfer inside the body of the nozzle and CHT between the nozzle and the flow are modeled. The cell size in the flame region is approximately 0.1 mm × 0.05 mm. At the nozzle, the near-wall refinement is used to resolve the thermal boundary layer at the flame attachment location with the smallest cell size of 5 µm. `chtMultiRegionFoam` solver is used, which allows CHT coupling. The fluid region is solved using the same equations as used in `reactingFoam`, except hydrostatic pressure is accounted for to evaluate the buoyancy effect. At fuel and air inlets, fixed mass fractions and velocities, and fixed flux conditions for pressure, are used.

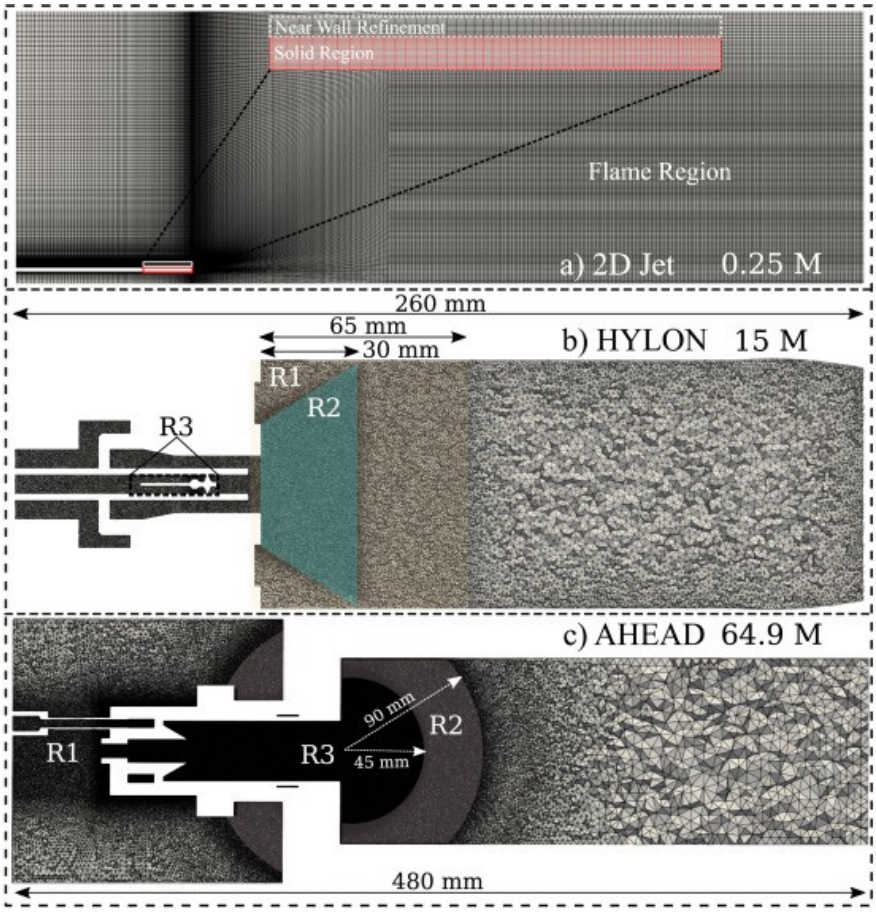

Download: Download high-res image (3MB)

Download: Download full-size image

Fig. 3. The mesh configuration setup and the refinement zones for (a) 2D jet, (b) HYLON burner, and (c) AHEAD burner. R refers to the refinement zone.

Multiple additional simulations with a larger domain size and various combinations of lateral and outlet pressure as well as velocity boundary conditions were first conducted. The numerically robust boundary condition settings that offer the closest results to those obtained with a substantially larger domain size are chosen for the present work. The air flow at the bottom and at the lateral boundary is set to a fixed value of 0.2 m/s, which is an estimate of the free stream velocity taken from the original work [23]. At the outlet, the total pressure and inlet-outlet velocity boundary conditions are used. To speed up convergence, heat transfer inside the solid parts of the nozzle is solved using a steady-state assumption, while the fluid flow is solved using a transient one. The simulation is run until the steady-state flame profile is reached. Since the temporal evolution of the flame is not considered, to arrive at the steady-state solution, the first-order Euler temporal discretization scheme is used.

2.4.3. Case 3: 3D turbulent non-premixed flame (HYLON, Flame A)

Third, the 3D turbulent non-premixed swirl-stabilized HYLON Flame A is studied. A volume rendering of the anchored stabilized flame represented by the instantaneous OH field is shown in Fig. 2c (top). As shown in Fig. 2c (bottom) the HYLON setup contains two swirling nozzles arranged coaxially to inject the oxidizer and fuel separately, as described in more detail by Marragou et al. [13]. Air is supplied through an annular channel (d_e = 22 mm) with a mass flow rate of 2.41 g/s. The air then passes through an air swirler consisting of eight 42° radially tilted cylindrical vanes (d_h = 4 mm) before getting injected into the combustion chamber through the annular inlet with an outer diameter d_E = 18 mm. Hydrogen is injected with a mass flow rate of 0.032 g/s via the inner tube (d_i = 6 mm) in which the hydrogen swirler is mounted. The global equivalence ratio resulting from the air and hydrogen inlet conditions is ϕ = 0.45. The Reynolds number based on the hydraulic diameter

of the injector annular cross section is 11 000. A recess height between the burner backplane (the lower wall of the combustion chamber) and the lip of the hydrogen tube is $Z_i = 4$ mm. Both air and hydrogen are injected at 300 K temperature. As mentioned by Marragou et al. [66] and Aniello et al. [12], the air and hydrogen swirlers generate a swirl number of $S_e = 0.60$ and $S_i = 0.65$ respectively.

Three tetrahedral meshes are employed to ensure grid independence of the results. Fig. 3b illustrates the mesh configuration for the HYLON burner, with the refinement zones R1-R3. The first mesh has a global cell size of 2 mm, reduced to 0.95 mm in the main vortex region (R1), and further refined to 0.45 mm in the flame region (R2). Additional refinement is applied around the hydrogen swirler (R3), where the cell size is 0.25 mm, resulting in a total of 15 million cells. In the second mesh, region R2 is refined down to 0.12 mm, increasing the total cell count to 21 million. A third mesh is also considered in the mesh sensitivity study, where the refinement in R2 is further reduced to yield small average cell size of 0.10 mm, resulting in a total of 24 million cells.

The used meshes are first tested in cold flow simulations (HYLON) using Pope's resolution criterion (M-criterion) [67] and the integral length scale to cell size ratio [68]. Also, the velocity profiles are provided on the coarsest grid resolution (15M). Further details can be found in the Supplementary Data file Sections S1.2 and S1.3.

The time step is controlled by the maximum Courant number of 0.8. At the inlet, fixed-values velocity, temperature, and species mass fractions are applied, while the zero-gradient condition is applied for the pressure. At the outlet, the pressure is set to the atmospheric value while zero gradient conditions are applied for the rest of the flow quantities. At the walls, the no-slip velocity boundary condition is used with the LES wall functions formulated for turbulent viscosity ν_t [69]. The wall heat transfer is modeled by imposing the reported experimental average temperature value of the external side of the combustion chamber and the measured temperature over the combustion chamber backplane [12]. The flow is first simulated for 150 ms to reach a statistically steady state, after which the field averaging is done for another 150 ms.

2.4.4. Case 4: 3D turbulent premixed flame (AHEAD)

Fourth, the 3D turbulent premixed swirl-stabilized AHEAD flame is studied at the global equivalence ratio $\phi = 0.6$. A volume rendering of the instantaneous OH contour is shown in Fig. 2d (top). Fig. 2d (bottom) shows the computational domain and the setup, which consists of five primary components: plenum, mixing chamber, combustion chamber, dilution air distributor, and fuel injection system, based on the experimental setup by Reichel et al. [14]. Air is introduced through the plenum, from where it is subdivided into three main paths to access the cylindrical mixing chamber: (1) axial inlet, providing the axial momentum (8 mm diameter), (2) 8 radial slits, creating tangential momentum (swirl motion), and (3) 12 dilution holes, preventing boundary layer flashback. Fuel is introduced through 16 fuel inlet ports into the mixing chamber; each fuel inlet port is 0.8 mm in diameter, encircling the truncated center body at the bottom of the mixing chamber. The diameter of the mixing chamber is 34 mm.

The mesh configuration is shown in Fig. 3c. Three tetrahedral meshes – coarse, medium, and fine – with 12.3, 28.6, and 64.9 million cells, respectively, are considered in the present study. The global cell size is set to 5 mm for all the meshes. The most refined region (R3) comprises the mixing chamber along with the flame anchoring region. The R1 and R2 refinement regions represent a gradual increase in mesh size from R3 to the global cell size. The R1 region represents the area before the axial air inlet, with a cell size set to 0.75 mm. The R3 cell size varies with each mesh: 0.75 mm for the coarse, 0.5 mm for the medium, and 0.35 mm for the fine mesh. The cell size in the R2 region is 1 mm for the coarse and medium meshes and 0.65 mm for the fine mesh. The used meshes are first tested in cold flow simulations (AHEAD) using Pope's resolution criterion (M-criterion) [67] and the LES-Index Quality (LES-IQ) [68] assessment methods, together with a quantitative analysis of mean velocity profiles. Further details can be found in the Supplementary Data file Sections S1.2 and S1.3.

The time step is fixed to 1 µs, which corresponds to the maximum Courant number of 0.6 in the domain. The boundary conditions for velocity, species mass fractions, and pressure are the same as in Case 3. The inlet air and hydrogen velocity/temperature are set to 3.696 m/s /453.15 K and 95.43 m/s/336.15 K, respectively. The Reynolds number based on the flow bulk velocity inside the mixing chamber is $Re = 75000$ The flow is strongly influenced by the high swirl number ($S = 0.9$), which is evaluated using the formula given in Eq. (17), similar to the study by Vignat et al. [70],

$$S = \frac{\int_0^R 2\pi uwpdr}{R\int_0^R 2\pi u^2 \rho dr}, \tag{17}$$

where R is the radius of the mixing tube, u is the mean axial velocity, w is the mean tangential velocity, and ρ is the mean density. At the combustion chamber walls, the adiabatic thermal boundary condition is assumed as detailed experimental measurements of the wall temperature profile for the AHEAD burner under the specific operating conditions are not available in the literature or public database [10]. The flow is modeled until 300 ms to reach a statistically steady state, after which the field averaging is done for another 50 ms.

The simulation setup incorporates a species-specific constant Lewis number transport model to account for the fast diffusion of light hydrogen atoms. Details regarding the calculation of species-specific Lewis numbers and the conditions used in the present simulations are provided in the Supplementary Data file Section S1.4. The turbulent Schmidt number (Sc_t) is set to 0.75, and the turbulent Prandtl number (Pr_t) to 0.85. To analyze the implemented transport models, six simulations are performed in total: three non-reactive flows to assess mesh independence and three reactive flows. The non-reactive simulations are presented in S1.3, and the reactive flow simulations are analyzed in Section 3.5. Additionally, one extra simulation is also carried out to analyze the mixture-averaged transport model and consistency between the two transport models. These results are provided in the Supplementary Data file Section S1.4.

3. Results and discussion

This section starts with the assessment of the implemented diffusion models and then, the numerical results from Cases 1–4 along with qualitative and quantitative discussions are demonstrated. For Case 1, the main purpose is to demonstrate the thermodiffusive flame structures along with a comparison to the theoretical dispersion relations derived from the linear stability theory. For Cases 2–4, verification/validation is carried out based on the available data from the literature.

3.1. Assessment of the diffusion models implementation (1D)

To verify the current implementation of the diffusion models (mixture-averaged and constant Lewis number) in `FickianTransportFoam`, the simulation results from `OpenFOAM` and `Cantera` are compared. The assessment study includes (1) a 1D freely propagating premixed flame and (2) a non-premixed counterflow flame.

Fig. 4(a–d) demonstrates the profiles of a freely propagating premixed hydrogen/air flame at $\phi = 0.5$, atmospheric pressure and 293 K temperature. The same domain size and mesh resolution of 100 cells per flame thickness are used in `Cantera` and `OpenFOAM`. For the species-specific constant Lewis number model, Lewis numbers are calculated as averages between the reactant and product sides in the premixed flame. The present implementation of the mixture-averaged model closely matches the `Cantera` simulation results for mass fractions Y_{H_2O}, Y_H, Y_{OH} and the heat release rate HRR. However, significant differences are observed in the prediction of H atom mass fraction and the heat release rate when assuming $Le = 1$ for all species due to the high mass diffusivity of the light species, as discussed in previous studies [72], [73].

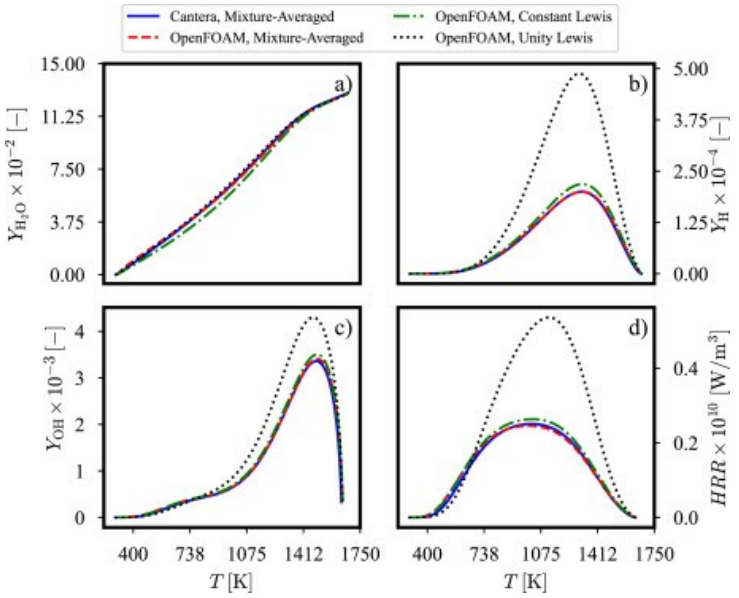

Download: Download high-res image (376KB)

Download: Download full-size image

Fig. 4. 1D freely propagating flame at the equivalence ratio of $\phi = 0.5$. Comparison between the mixture-averaged model from `Cantera` and the present implementation of the mixture-averaged model and constant Lewis number (Le_k) approach in `FickianTransportFoam`. (a) H_2O mass fraction (b) H mass fraction (c) OH mass fraction and (d) the heat release rate in the temperature space. The results from the unity Lewis number assumption are provided for comparison.

Fig. 5 shows the results for the present `FickianTransportFoam` mixture-averaged implementation along with the respective results from `Cantera` for a non-premixed counterflow flame at atmospheric pressure, temperature 293 K, and strain rate $\chi = 20\ s^{-1}$. The same mesh resolution of $\Delta x = 50\ \mu m$ is used for both cases. The species-specific constant Lewis number approach is ruled out of the comparison, as getting an accurate Lewis number definition across the non-premixed flame may not be straightforward [74]. The results show that the prediction of the non-premixed flame structure from both models aligns well with the mixture-averaged results from `Cantera`. Differences may be attributed to different governing equations: `Cantera` uses one-dimensional (1D) non-premixed counterflow flame equation, and `OpenFOAM` uses general set of two-dimensional equations.

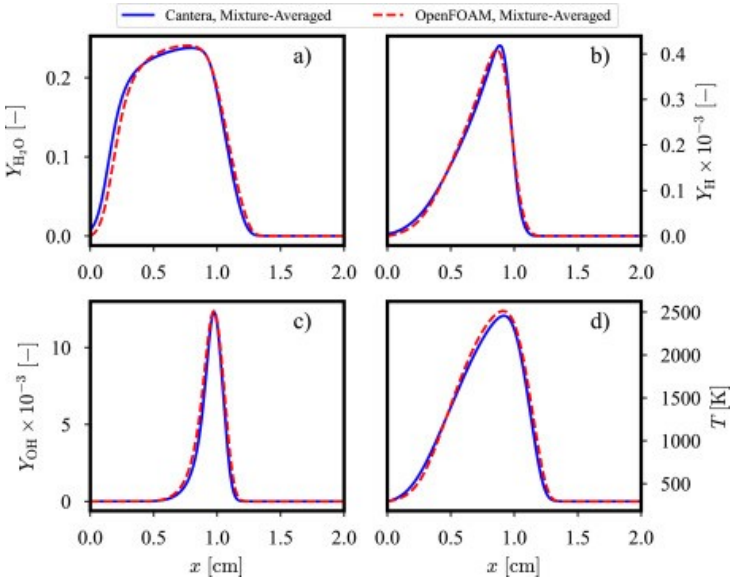

Download: Download high-res image (348KB)

Download: Download full-size image

Fig. 5. Non-premixed counterflow flame at atmospheric conditions. The comparison of two different transport models in predicting the flame structure at the strain rate 20 $\mathbf{s^{-1}}$. (a) H_2O mass fraction, (b) H mass fraction, (c) OH mass fraction, and (d) the flame temperature across the computational domain.

3.2. Case 1: 2D laminar freely propagating premixed flame

Case 1 represents a temporally evolving thermodiffusively unstable planar flame at $\boldsymbol{\phi = 0.5/1.0/1.5}$. Fig. 6 shows the temporal evolution of the flame that is initiated with a 1D laminar flame profile with a small spatial sinusoidal perturbation (at $\boldsymbol{\phi = 0.5}$). It can be noticed from Fig. 6 that due to the unstable character of lean hydrogen flames, the harmonic perturbation amplifies rapidly within a couple of flame times ($\boldsymbol{\tau = \delta_L^o / S_L^o}$) and forms a well-structured periodic flame front where the initial wavelength $\boldsymbol{\lambda_{max}}$ pattern can still be clearly observed. After approximately 40–50 flame times, the structured periodic pattern starts to break and irregular structures are clearly seen at time $75\boldsymbol{\tau}$. The irregular structures evolve and merge, eventually forming two large flame fingers shown at time $150\boldsymbol{\tau}$. The observed flame cellular micro-structures are consistent with hydrogen flame front dynamics described in the literature [4], [75].

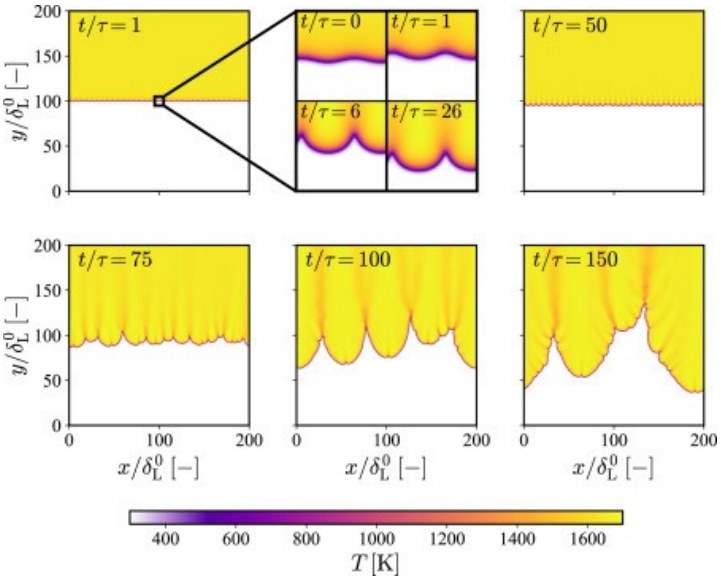

Download: Download high-res image (364KB)

Download: Download full-size image

Fig. 6. Temporal evolution of temperature field of a 2D freely propagating lean ($\boldsymbol{\phi = 0.5}$) hydrogen flame at ambient conditions ($\boldsymbol{T = 298\ \mathrm{K}, p = 1\ \mathrm{bar}}$).

The relationship between the linear growth rate $\boldsymbol{\omega}$ and the perturbation wavelength, $\boldsymbol{\lambda}$, is examined by conducting a set of simulations within a smaller domain in which the height corresponds to $\boldsymbol{\lambda}$. The purpose of the smaller domain simulations is to extract the linear growth rates of the perturbation. Fig. 7a shows the normalized growth rate ($\boldsymbol{\omega \cdot \tau}$) for different normalized wavenumbers $\boldsymbol{k = 2\pi/\lambda}$, i.e. the dispersion relationship $\boldsymbol{\omega(k)}$. A cubic spline is fitted to the simulation points and the results are compared with the analytical dispersion relations developed by Matalon et al. [71]. It is noted that the simulation trends agree well with the analytical profiles for the stoichiometric and rich cases. For the lean case, the analytical dispersion relation cannot model the stabilization taking place at shorter wave lengths correctly for flames with Lewis number below the critical number, due to lack of the underived higher-order terms, which explains the difference between numerical and analytical solutions. Fig. 7b shows a significant increase in the consumption speed of the large-scale flame, which is evaluated as $\boldsymbol{S_c = -\frac{1}{\rho_u Y_{H_2,u} A} \int \dot{\omega}_{H_2}\, dA}$ (where $\boldsymbol{A}$ is the cross sectional area, and subscript $\mathbf{u}$ stands for unburnt), meaning that the propagation speed of the present unstable flame front is more than 2.5 times higher than the corresponding $\boldsymbol{S_L^o}$ mainly due to the increased flame area. Finally, Fig.

7(c,d) show the probability density functions of mixture fraction Z and heat release rate with respect to the progress variable $C_{H_2} = 1 - Y_{H_2}/Y_{H_2,inlet}$, where Z is defined based on Bilger's definition [76]. The conditional means are compared with the corresponding one-dimensional solution. The probability density functions show the different range of combustion conditions present in the wrinkled flame front. The difference between conditional mean and 1D unstretched solution is attributed to the thermodiffusive effects, which change the local equivalence ratio. In conclusion, the usage of the transport models in the `FickianTransportFoam` library enables capturing the expected trends of the linear growth phase for different values of ϕ. For large-scale simulations, the thermodiffusively unstable flame structure and the increased fuel consumption speed are captured. Furthermore, the difference between the conditional mean of the unstable 2D and the 1D flame structure in the progress variable space indicates that the thermodiffusive effect is captured. It is noted that these 2D simulations could serve as useful initial benchmark simulations for anyone starting research on computational hydrogen combustion instabilities (see objective 1).

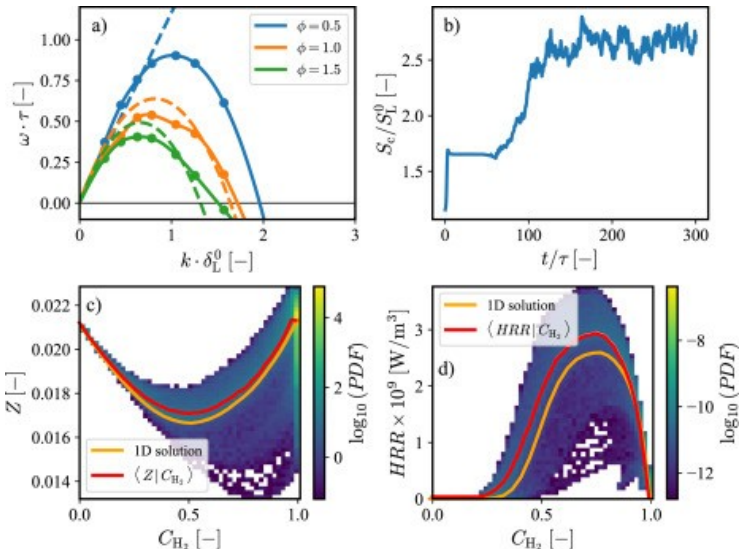

Download: Download high-res image (440KB)

Download: Download full-size image

Fig. 7. Simulations of 2D freely propagating hydrogen flames at ambient conditions $(T = 298\ \mathrm{K}, p = 1\ \mathrm{bar})$. (a) Comparison between numerically calculated dispersion relations (solid lines) and dispersion relation by Matalon et al. [71] (dashed line) at $\phi = 0.5/1.0/1.5$. (b) Normalized fuel consumption speed of lean hydrogen flame ($\phi = 0.5$). (c–d) Joint probability density functions of a lean ($\phi = 0.5$) hydrogen flame with respect to the progress variable C_{H_2}.

3.3. Case 2: 2D axisymmetric laminar non-premixed jet flame

Case 2 represents a 2D laminar non-premixed jet flame, simulated in an axisymmetric domain (wedge-type mesh). The flame has already been investigated experimentally and numerically by Cheng et al. [23]. Fig. 8 shows a fully developed flame that has reached the steady-state condition. The temperature field is shown on top, while the OH mass fraction is shown on the bottom of the figure. The overall shape of the flame qualitatively agrees with the laser-induced predissociative fluorescence (LIPF) OH specie image reported in the experimental study. It is observed that the flame attaches to the nozzle approximately 0.7 mm upstream of the nozzle tip, due to the upstream diffusion of hydrogen outside the nozzle. A closer examination of the nozzle area (see inset) shows the temperature field obtained by the CHT solution. The numerical results indicate nozzle temperature levels above 500K at the tip, which significantly preheats the H_2 fuel stream boundary layers. This observation is in line with the findings of the original work by Cheng et al. [23].

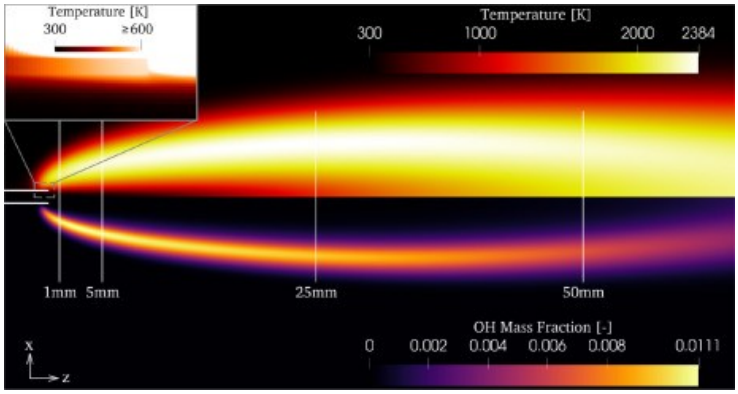

Download: Download high-res image (268KB)

Download: Download full-size image

Fig. 8. 2D axisymmetric laminar non-premixed jet flame. Flame temperature (top) and OH mass fraction (bottom) fields. Experimental measurement locations are shown with white vertical lines. The additional zoom panel on the top left shows the temperature distribution of the nozzle wall offered by the CHT solution. The zoom also reveals the preheating of the hydrogen boundary layers. Note that the picture is rotated, the nozzle is vertical in both experimental and numerical setups.

Fig. 9 shows a comparison of the temperature and mass fraction profiles with the experimental data at the measurement locations (see Fig. 8). In general, the radial profiles appear to be in relatively good agreement with the experimental data. However, at the first two measurement locations ($z = 1\,\mathrm{mm}$ and $z = 5\,\mathrm{mm}$) the flame width is underpredicted, as in the modeling results of Cheng et al. [23]. In our simulations, the peak location of OH is underpredicted by 20% in the present study while the location of the peak is underpredicted by up to 15% in the work by Cheng et al. [23]. In the present simulations, the peak OH concentration value is overpredicted at $z = 1\,\mathrm{mm}$ by 14%, at $z = 5\,\mathrm{mm}$ by 3%, at $z = 25\,\mathrm{mm}$ by 7.5%, and further downstream at $z = 50\,\mathrm{mm}$ by 30%. Overprediction of OH peak values might be an indication of overestimation of the OH production rates by the reduced chemical kinetic mechanism by Capurso et al. in the present conditions. The underprediction of O_2 and the overprediction of H_2O on the fuel-lean side of the flame suggests that the mixing and the corresponding reaction rates can be underestimated. Further downstream ($z \geq 25\,\mathrm{mm}$), the agreement for O_2 and H_2O improves, and the simulated profiles match the experimental data relatively well.

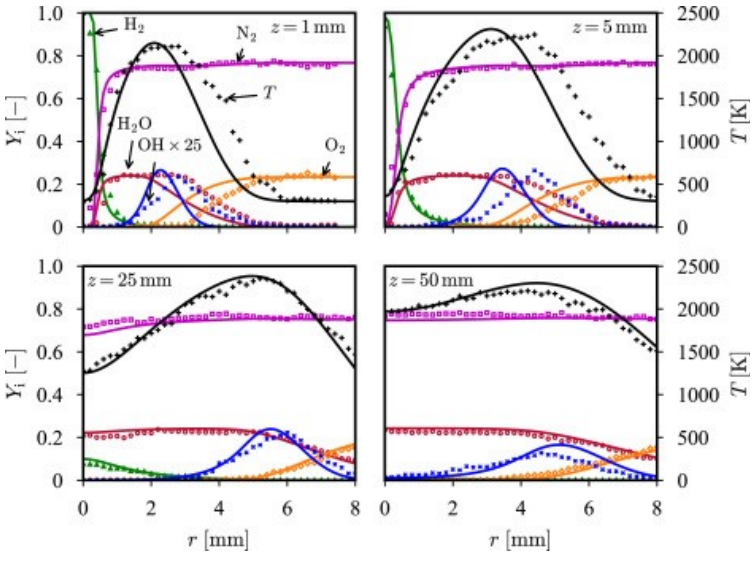

Download: Download high-res image (602KB)

Download: Download full-size image

Fig. 9. 2D axisymmetric laminar non-premixed jet flame. Radial profiles of temperature, major species and OH mass fractions at different sampling locations compared to the experimental data. Solid lines – simulated data,

symbols – experimental data.

In the reference work, it was assumed that the main cause of the aforementioned differences was the underestimation of the diffusion mass transport, which in turn could be caused by possible inaccuracies in the diffusion transport data for H and H_2. Overall, the good qualitative and quantitative agreement between the simulation results and the experimental data shows that the present numerical setup is suitable for modeling laminar non-premixed flames with CHT.

3.4. Case 3: 3D turbulent non-premixed flame (HYLON, Flame A)

Case 3 represents a 3D turbulent non-premixed swirling flame, i.e. the HYLON Flame A configuration. Fig. 10a shows a comparison between the time-averaged reactive flow axial velocity fields for the experiments (left) [12] and the present LES (right). Despite small differences, the simulated flow structure, along with the vortex locations including the central recirculation zone (CRZ) and the outer recirculation zone (ORZ), are in good agreement with the experimental data. Fig. 10b shows the mean normalized Abel-deconvoluted OH^* chemiluminescence signal from the experiments (left) next to the present LES for which the normalized time-averaged heat release rate distribution $\boldsymbol{HRR_{norm}}$ is illustrated (right). The height of the flame in addition to the intensity and location of both reaction fronts I and II are well captured in the present simulations. The numerical results indicate that the main reaction front anchors to the hydrogen injector's lip, which is consistent with the observations from previous experimental and numerical works on Flame A [12], [13]. The lower part of the figure shows the instantaneous contours of the gas temperature (c) and the heat release rate (d). From Fig. 10c and d, it is evident that the hottest gases are not directly located at the main heat release front (I). Instead, the temperature peaks are observed in the secondary reaction front (II) within the wake of the hydrogen injector at the edge of the CRZ. This could be explained by the dynamics of the hot gases, where the CRZ provides a longer residence time for the gases at the secondary reaction front, leading to an increase in the gas temperature.

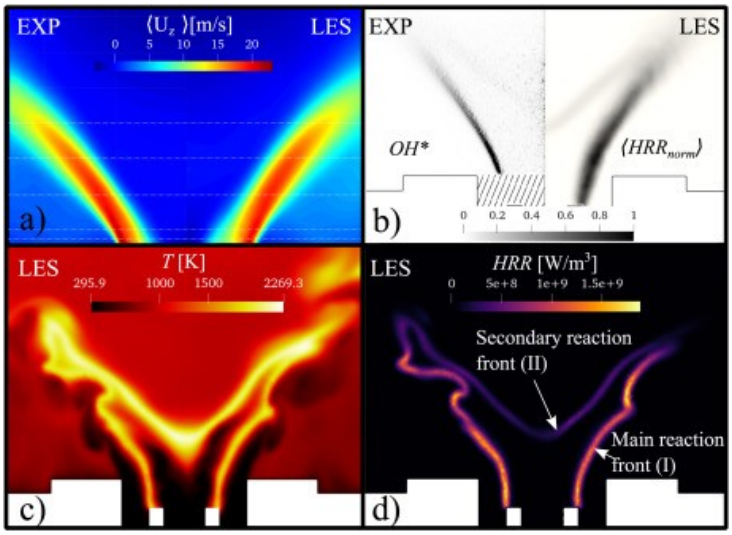

Download: Download high-res image (491KB)

Download: Download full-size image

Fig. 10. HYLON flame A. (a) A comparison between the experimental PIV measured mean axial velocity [14] next to the LES results from the current work. (the dashed lines show the location where the data is plotted in Fig. 11) (b) The time-averaged experimental normalized Abel-deconvoluted $\boldsymbol{OH^*}$ chemiluminescence signal [14] compared to the time-averaged normalized heat release (normalized by the maximum $\langle \boldsymbol{HRR_{max}} \rangle$ in the domain) taken from the LES results. (c) The instantaneous temperature contours. (d) The instantaneous heat release rate.

To provide a quantitative comparison, Fig. 11(a–d) displays the time-averaged radial distribution of the axial

(a,b) and radial (c,d) velocity components at four different downstream locations. The comparison between the simulations and the experimental data indicates that the mean velocity profiles are mesh-independent for the three studied meshes. The numerical and experimental profiles match well regarding the peak values and the flow gradients at the inner and outer shear layers. Due to the lack of quantitative experimental data for the gas temperature and the species concentration, the numerical results from different meshes (15M, 21M, and 24M) are compared in Fig. 11(e–h). It can be observed that the mean gas temperature and OH mass fraction are more sensitive to the mesh refinement along the flame than the velocities. The profiles have the same trends, and the peak values match at 10 mm downstream location. In conclusion, the present results indicate that the numerical setup captures the main characteristics of the turbulent swirling non-premixed flame, as demonstrated by both qualitative and quantitative validations.

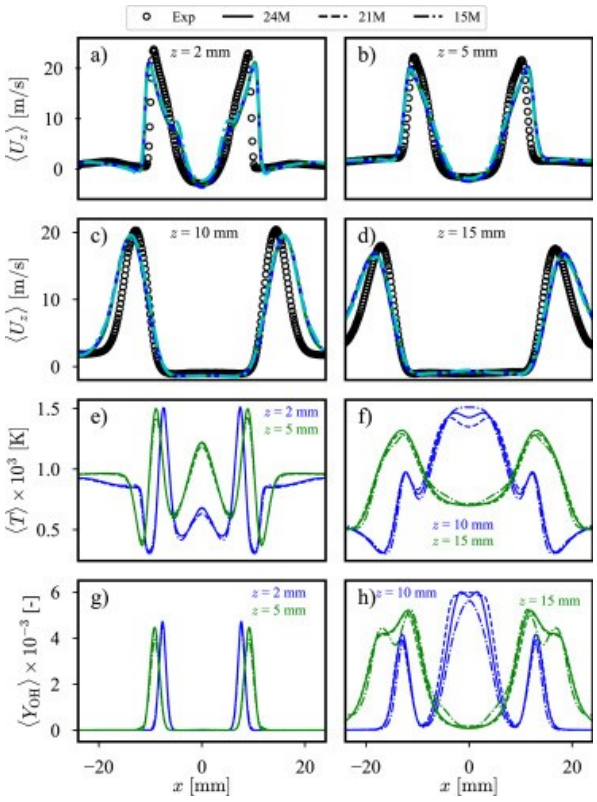

Download: Download high-res image (706KB)

Download: Download full-size image

Fig. 11. HYLON flame A. The time- and circumferential-averaged axial (a,b) and radial (c,d) velocity profiles shown from two different downstream locations compared to the experimental data [14]. The mesh sensitivity of two meshes is shown for velocities (a–d) as well as temperature and OH mass fraction (e,f).

3.5. Case 4: 3D turbulent premixed flame (AHEAD)

Finally, Case 4 represents a 3D turbulent premixed swirling flame, i.e. the AHEAD configuration. The time-averaged axial and radial components of the velocity field are compared to the PIV data from Reichel et al. [16] in Fig. 12(a,b). As observed from the velocity field in Fig. 12(a,b), the present LES predicts similar axial and radial velocity patterns as observed in the experiments. However, in comparison to Case 3, the deviations in the velocity fields are more obvious. There could be various reasons for such differences: (1) The complex arrangement of the mixing system (airflow splitting through a swirler and an axial air inlet close to the fuel inlets. (2) As noted also by Capurso et al. [20], the peak axial inlet velocities (see Fig. 2) are relatively high (Mach number $\approx \mathbf{0.55}$) which could pose certain limitations for solving this case with a pressure-based solver. (3) Additionally, finite grid resolution in LES as well as the chosen TCI model could affect the results e.g. in the central recirculation zone and reaction zones. The effect of the geometric complexities can be evaluated when looking at the non-reactive validation simulation of the same setup, presented in the Supplementary Data file

Section S1.3, which shows better agreement with the experimental data compared to the reactive validation. From the simulated velocity field, it is evident that the CRZ shifted towards the mixing chamber, which is caused by the higher magnitude of the axial velocity predicted in the ORZ as compared to experimental results upon the vortex breakdown.

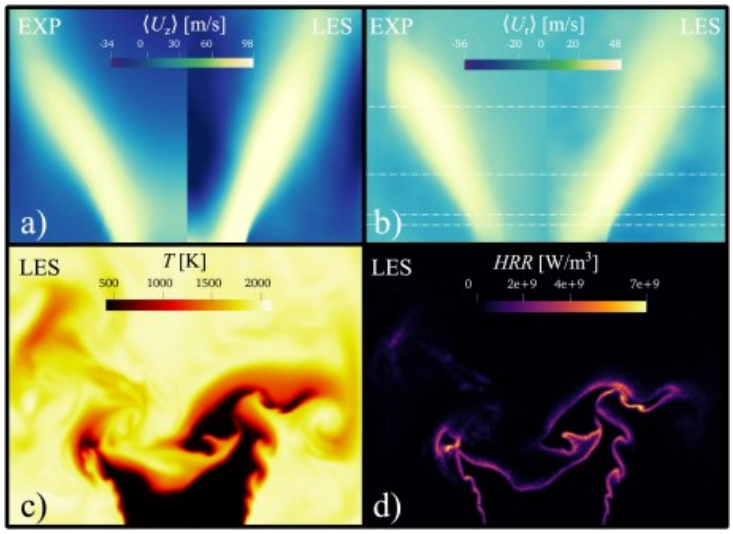

Download: Download high-res image (463KB)

Download: Download full-size image

Fig. 12. AHEAD flame. The time-averaged axial (a) and radial (b) velocities between present LES and experimental PIV measurements by Reichel et al. [18] (the dashed lines show the location where the data is plotted in Fig. 13). The instantaneous gas temperature (c) and HRR (d) from the present LES are also shown to indicate stabilized turbulent premixed flame location.

Four downstream velocity profiles compared to the experimental data as well as the LES results of Capurso et al. [20] are shown in Fig. 13(a–d) to offer more insight into the quantitative differences. Along these profiles, the shaded blue region is obtained by extracting simulation data above and below the profile curves at locations $z \pm 2$ mm to quantify the spatial sensitivity to the sampling location in the numerical results. It is clear that the flow along the center of rotation is not fully captured in the present LES, which was also the case in the previous study by Capurso et al. [20]. The present LES seems to align the best with the velocity profiles (sim. and exp.) at the upstream location, where the flame is stabilizing, which aligns with the observations by Mira et al. [18]. In general, the velocity distribution across the flame front appears to be in a reasonable agreement with the LES of Capurso et al. [20], while there are more discrepancies between the simulations and experimental data further downstream ($z = 40$ mm). The uncertainty between the experimental and computed numerical results in the shear layer and ORZ regions closely follows the experimental data and remains within the $z \pm 2$ mm shaded region. In the CRZ, the numerical results deviate from the experimental measurements, and the shaded blue region show very large changes in velocity variations. Such deviations in velocity profiles are also observed in the reference numerical results computed by Capurso et al. [20]. Since quantitative experimental data for temperature are not available, the time-averaged temperature and mole fraction of OH from different mesh resolutions (12.3M, 28.6M, 64.9M) are presented in Fig. 13(e–h). It can be seen that the temperature profiles at different locations for medium and fine meshes are relatively close to one another, and the trends in all meshes are similar. The changes in the mole fraction of OH at $z = 5.4$ mm align with each other in the shear layer between the CRZ and the ORZ. The effect of CRZ penetrating towards the mixing chamber, which is highlighted from the velocity profiles, has an effect on the OH fraction. In the ORZ, there is a noticeable change in OH mole fraction between the meshes. With each mesh refinement, the level of the OH mole fraction is reduced in the ORZ, but the variance decreases with increasing resolution, indicating convergence. At the height of 40.8 mm, it can be seen that the OH fraction profiles from the medium and fine meshes show relatively close trends and the variance between meshes is smaller than at the height of 5.4 mm.

In conclusion, the present LES (WALE+PaSR) and `FickianTransportFoam` library is considered to predict the main characteristics of such a stabilized premixed hydrogen flame. The numerical observations indicate that Case 4 (3D premixed) appears the most challenging case to simulate out of the studied four flame types.

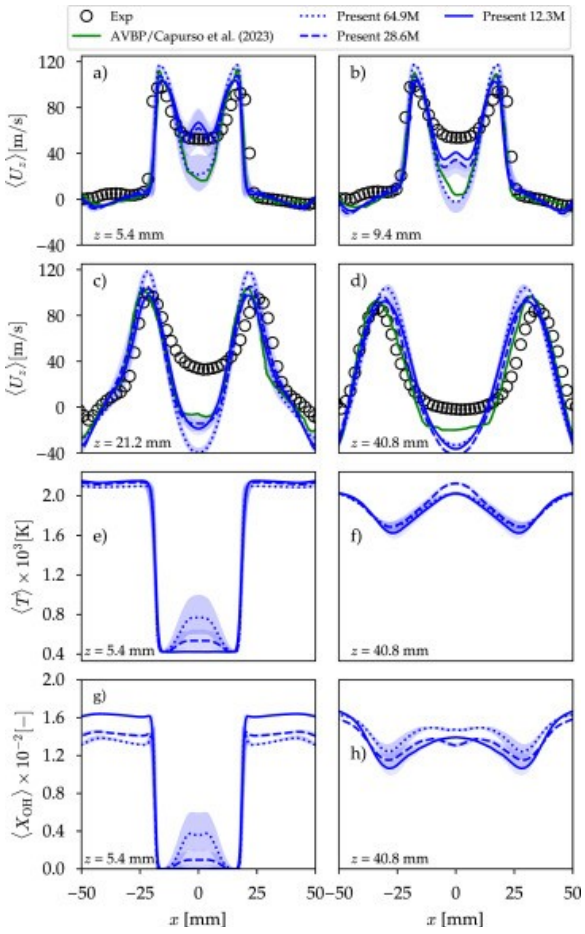

Download: Download high-res image (691KB)

Download: Download full-size image

Fig. 13. AHEAD flame. The time-averaged axial (a–d) velocities shown from four different downstream locations along with a comparison with the experimental data as well as the LES data by Capurso et al. [22]. The mesh sensitivity is shown as well for temperature (e,f) and OH mole fraction (g,h). The blue shaded region corresponds to the bounds taken by sampling from locations $z \pm 2$ mm around the exact sampling locations. (For interpretation of the references to color in this figure legend, the reader is referred to the web version of this article.)

3.6. Computational speed-up

Next, we illustrate the speed-up benefits of `DLBFoam` with respect to the standard `OpenFOAM-v10` in the pure hydrogen combustion cases (1–4). For consistency, the absolute and relative tolerances of the chemistry ODE solver are set to 10^{-10} and 10^{-6} respectively in all four cases similar to previous investigations by Morev et al. [27]. Starting from a time when the flames are well-developed, the speed-up benchmark simulations are run for 100 fixed timesteps, and the speed-up is calculated as the ratio of execution times between the standard `OpenFOAM` and `DLBFoam` approaches. The number of time steps has to be limited to 100 due restrictions in the used computational infrastructure limiting maximum runtime to 36 h. For all benchmarks except AHEAD flame with standard `OpenFOAM` (discussed below) 100 time steps can be executed within 36 h. Also, since `DLBFoam` does rebalancing operation every time step, the corresponding overhead is uniformly distributed across all time steps, and therefore the rebalancing does not affect the speed-up calculation. As in the previous work [27], all benchmarks are performed on the Mahti supercomputer at CSC - Finnish IT Center for Science. Mahti has **1404** nodes each with two **64**-core 2.6GHz (boost up to 3.3GHz) AMD Rome 7H12 CPUs. All nodes are

connected to the inter-node communication network with 200GB/s links [77]. OpenFOAM is compiled using gcc compiler version 11.2.0 and OpenMPI version 4.1.2.

Fig. 14a represents the benchmark results for cases 1–4. In Case 1, the mean execution times are estimated starting from the time when the flame instabilities are fully developed ($t/\tau = 270$). The results indicate approximately one order of magnitude speed-up, showing good scaling of the speed-up results for a larger number of processors despite relatively small mesh size (4 million cells). In Case 2, the execution times are estimated starting from a time when the flame height is approximately 80% of the steady-state flame height. The speed-up has the same order of magnitude as in Case 1. However, due to very small mesh size (250000 cells), with the increase of the number of processors communication overhead for linear solvers starts to significantly influence the computation time, thus worsening the obtained speed-up numbers with the increase of the number of processors. In Case 3, the comparison is done by starting the case from a fully developed state (at $t = 250\,\mathrm{ms}$), when the swirling flame is stabilized and the CRZ/ORZ are formed. The speed-up is also in the order of 10 with a good scaling for larger number of processors. Finally, Case 4 represents the most computationally expensive case. As for Case 4, the benchmark is performed when the flame is in a statistically steady state ($t = 350\,\mathrm{ms}$). Due to very long integration times for the standard OpenFOAM, this reference case is not even able to finish within the supercomputer's job limit of 36 h. Thus, only data up to iterations 7, 13, and 31 are calculated for 128, 256, and 640 cores, respectively. It is observed that the variation of computational time spent on a single iteration does not change substantially. Given also that DLBFoam does load rebalancing every time step, we consider it reasonable to calculate speed-up values based on smaller number of iterations. In Case 4, the results show significantly larger speed-up factors, compared to the previous case, approximately by one order of magnitude. There could be various explanations for the high speed-up such as the domain decomposition within this computational architecture. However, our numerical tests indicate that the PaSR model, when compared against the perfectly-stirred reactor model (no TCI), may affect the computational time in general. This could be related to the variations in chemical stiffness due to scaling of the reaction source terms by the κ factor (see Eq. (12)). Such a scaling could change the chemical balance in the system (e.g. relative importance of diffusion vs. chemistry) which could change the chemistry significantly. However, we did not study these aspects further in the present study.

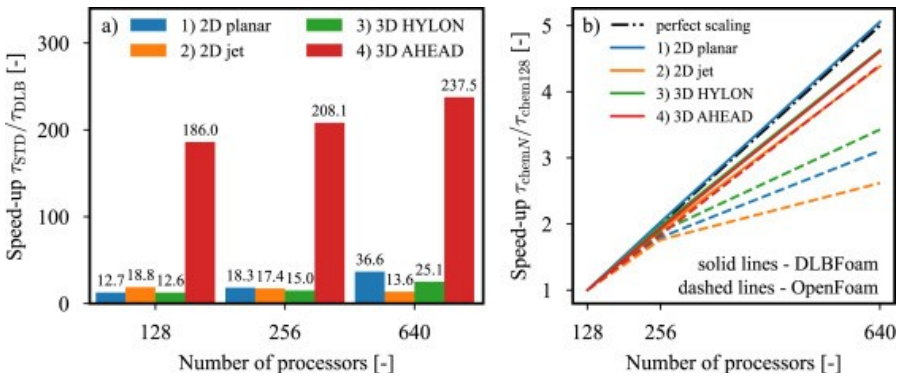

Download: Download high-res image (344KB)

Download: Download full-size image

Fig. 14. (a) A comparison of the computational speed-up, defined as the ratio between the solver total execution time of the standard OpenFOAM and DLBFoam approaches. b) Strong scaling of the chemistry problem solution time for the standard OpenFOAM (dashed lines) and DLBFoam (solid lines) approaches compared to the perfect scaling.

Fig. 14b shows the strong scaling of the investigated approaches, defined as the ratio between the chemistry solution time for a given number of processors and the chemistry solution time for **128** processors. For all investigated cases, the strong scaling with DLBFoam approaches the perfect linear scaling, which is not observed for the standard OpenFOAM.

As a remark, we note that the tolerances of the chemistry integrator chosen for the benchmark are relatively tight. As shown in the previous work, the tolerance may have a large effect on the chemistry integration time for the standard `OpenFOAM` [27]. However, this setting enables a direct comparison of the speed-up factors with those investigated previously for larger chemical kinetic mechanisms for fossil fuels. The important observation here is that even for small hydrogen mechanisms, the same orders of magnitude for speed-up could still be observed using `DLBFoam`.

4. Conclusions

In the present work, the usage of `OpenFOAM` and the dynamic load balancer `DLBFoam` library for CFD simulations of different pure H_2 flame configurations have been presented and explored. The implementation of the new diffusion model library `FickianTransportFoam` into `OpenFOAM`, including two transport models (the species-specific constant Lewis number and the mixture-averaged model), has been discussed. The contribution and findings of the paper can be listed as follows:

1. A newly developed diffusion model library `FickianTransportFoam` was presented, including two diffusion models: mixture-averaged and species-specific constant Lewis number. An important contribution of the present model is the incorporation of the correction velocity approach in `OpenFOAM` and the demonstration of the applicability of `FickianTransportFoam` for various test cases.

2. The newly developed library was verified against `Cantera` with 1D freely-propagating premixed and non-premixed counterflow flame cases.

3. The functionality of the `FickianTransportFoam` library was demonstrated for two premixed and two non-premixed hydrogen flame setups with increasing levels of complexity. The new library was noted to be computationally robust and compatible with LES's as well.

4. For the 2D premixed flame, formation of thermodiffusive instabilities was demonstrated and relatively good agreement between numerical and analytical dispersion relationships was observed for the linear growth phase of the instabilities.

5. For the 2D axisymmetric non-premixed laminar jet flame case, the radial species profiles showed comparable agreement between previous numerical and experimental observations.

6. For the 3D HYLON flame A (non-premixed) case, the results using the mixture-averaged diffusion model were shown to be insensitive to the chosen grid.

7. For the 3D AHEAD flame (premixed) case, the results using the species-specific constant Lewis number approach were shown to be relatively grid independent although quite strong sensitivity of results to downstream sampling location was observed in the CRZ region. However, the results were comparable with previous computational observations and consistent with the mixture-averaged modeling approach, as shown in the Supplementary Data file Section S1.4.

8. The test cases 1–4 were used to benchmark and test the benefits of the previously introduced load-balancer `DLBFoam` using `FickianTransportFoam` against standard `OpenFOAM`. We report speed-ups in the order of one to two orders of magnitude. The benefit of `DLBFoam` in hydrogen context has not been discussed earlier and observing relatively high speed up for hydrogen was non-obvious (small mechanism).

9. Finally, the source code and the case setup files used in this study are made publicly available.

There are also various limitations in the present study. For example, we did not investigate other LES models than the WALE model or other TCI models than PaSR in the AHEAD case. These aspects could be further studied in the future. Furthermore, the present version of the library did not include the Soret diffusion model which is part of our future work. The results of all test cases showed the ability of the `FickianTransportFoam` library to predict various features of H_2 flame dynamics for different combustion modes. Importantly, the source code and the case setup files used in this study are made publicly available.

CRediT authorship contribution statement

Ali Haider: Writing – review & editing, Writing – original draft, Visualization, Validation, Software, Investigation. **Ilya Morev:** Writing – review & editing, Writing – original draft, Visualization, Validation, Software, Methodology, Investigation. **Aleksi Rintanen:** Writing – review & editing, Writing – original draft, Visualization, Validation, Software, Methodology, Investigation. **Zin Shahin:** Writing – review & editing, Writing – original draft, Visualization, Validation, Software, Investigation. **Parsa Tamadonfar:** Writing – review & editing, Supervision. **Shervin Karimkashi:** Writing – review & editing, Supervision. **Armin Wehrfritz:** Writing – review & editing, Methodology, Funding acquisition. **Ville Vuorinen:** Writing – review & editing, Supervision, Funding acquisition, Conceptualization.

Declaration of competing interest

The authors declare that they have no known competing financial interests or personal relationships that could have appeared to influence the work reported in this paper.

Acknowledgments

This study is financially supported by Business Finland, grant number 7578/31/2022 “HENNES”. Ville Vuorinen would like to acknowledge the support of the COST action CYPHER CA22151. Zin Shahin acknowledges financial support from Merenkulun säätiö, Walter Ahlström säätiö, and Tekniikan Edistämissäätiö. Ali Haider acknowledges Merenkulun säätiö for financial support and Ennova Technologies for providing the meshing tool license. Parsa Tamadonfar would like to acknowledge the Research Council of Finland (grant number 332835) and the Hi-EFECTS project by Nordic Energy Research (project number 172460). Shervin Karimkashi would like to acknowledge the Research Council of Finland project Wet-HyAm (grant number 361479). We highly appreciate the computational resources provided by CSC - Finnish IT Center for Science, which enabled performing the large-scale numerical simulations of this study.

Appendix A. Supplementary data

Download all supplementary files included with this article What's this? ↗

The following is the Supplementary material related to this article.

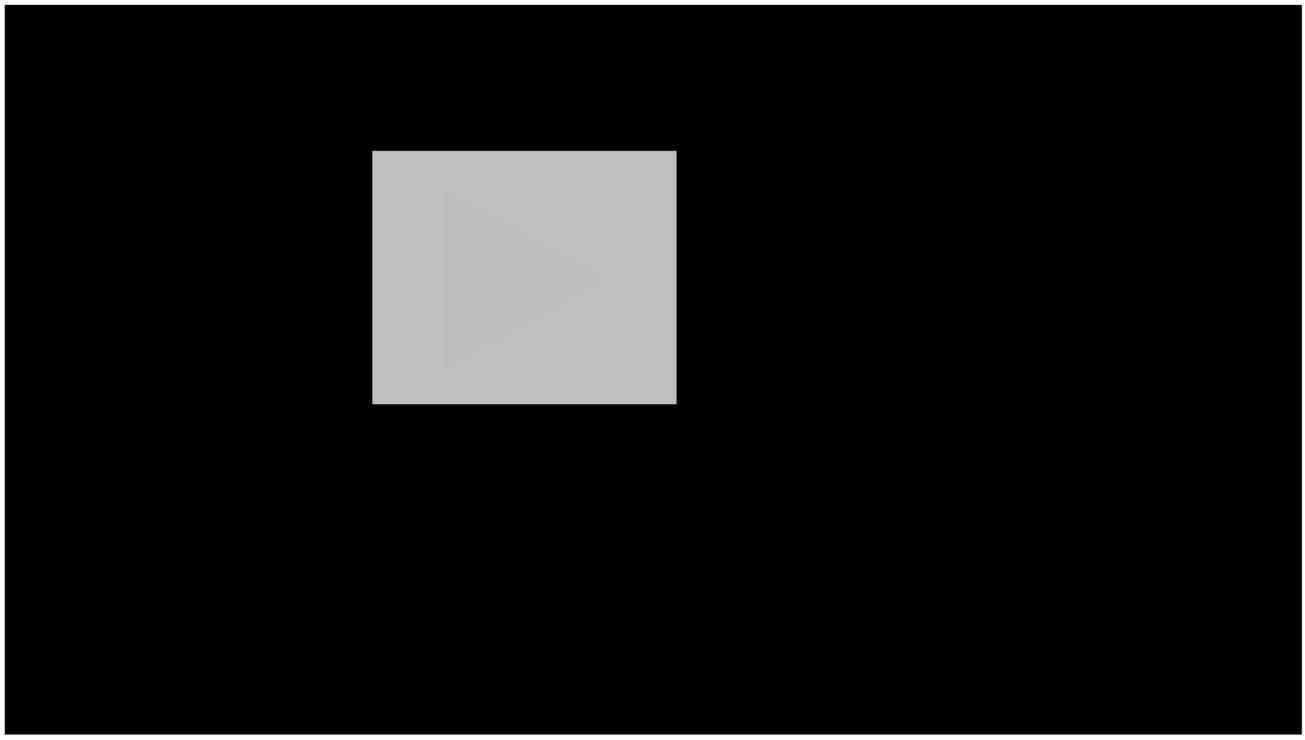

0:00 / 0:58 Speed: 1x *Paused*

Download: Download video (6MB)

Video S1.

Download: Download Acrobat PDF file (6MB)

MMC S2.

Recommended articles

Data availability

The data that support the findings of this study in addition to the presented FickianTransportFoam library are openly available in GitHub repository at https://github.com/Aalto-CFD/DLBFoam-Hydrogen-Tutorials ↗ and https://github.com/Aalto-CFD/FickianTransportFoam ↗ Refs. [46], [47].

References

[1] A. Risco-Bravo, C. Varela, J. Bartels, E. Zondervan
From green hydrogen to electricity: A review on recent advances, challenges, and opportunities on power-to-hydrogen-to-power systems
Renew Sustain Energy Rev, 189 (2024), Article 113930
View PDF View article View in Scopus ↗ Google Scholar ↗

[2] S. Marragou
Flow structure, mixing, flame stabilization and pollutant emissions from a coaxial dual swirl CH_4 /H_2 /Air injector
[PhD Thesis]
Institut National Polytechnique de Toulouse - INPT (2023)

Google Scholar ↗

[3] K.T. Møller, T.R. Jensen, E. Akiba, H.-w. Li
Hydrogen - A sustainable energy carrier
Prog Nat Sci: Mater Int, 27 (1) (2017), pp. 34-40
View PDF View article View in Scopus ↗ Google Scholar ↗

[4] L. Berger, A. Attili, H. Pitsch
Intrinsic instabilities in premixed hydrogen flames: parametric variation of pressure, equivalence ratio, and temperature. Part 2 – Non-linear regime and flame speed enhancement
Combust Flame, 240 (2022), Article 111936
View PDF View article View in Scopus ↗ Google Scholar ↗

[5] L. Berger, A. Attili, H. Pitsch
Intrinsic instabilities in premixed hydrogen flames: Parametric variation of pressure, equivalence ratio, and temperature. Part 1 - Dispersion relations in the linear regime
Combust Flame, 240 (2022), Article 111935
View PDF View article View in Scopus ↗ Google Scholar ↗

[6] N. Peters
Turbulent combustion
Cambridge monographs on mechanics, Cambridge University Press, Cambridge (2000)
Google Scholar ↗

[7] L. Berger, A. Attili, H. Pitsch
Synergistic interactions of thermodiffusive instabilities and turbulence in lean hydrogen flames
Combust Flame, 244 (2022), Article 112254
View PDF View article View in Scopus ↗ Google Scholar ↗

[8] H. Pitsch
The transition to sustainable combustion: Hydrogen- and carbon-based future fuels and methods for dealing with their challenges
Proc Combust Inst, 40 (1–4) (2024), Article 105638
View PDF View article View in Scopus ↗ Google Scholar ↗

[9] L. Berger, A. Attili, M. Gauding, H. Pitsch
Effects of Karlovitz number variations on thermodiffusive instabilities in lean turbulent hydrogen jet flames
Proc Combust Inst, 40 (1) (2024), Article 105219
View PDF View article View in Scopus ↗ Google Scholar ↗

[10] TNF workshop: https://tnfworkshop.org/ ↗.
Google Scholar ↗

[11] Launch of clean aviation's working group on validation of hydrogen flame numerical simulations:
(2023)
https://www.clean-aviation.eu/launch-of-clean-aviations-working-group-on-validation-of-hydrogen-flame-numerical-simulations ↗
Google Scholar ↗

[12] A. Aniello, D. Laera, S. Marragou, H. Magnes, L. Selle, T. Schuller, T. Poinsot
Experimental and numerical investigation of two flame stabilization regimes observed in a dual swirl H_2 -air coaxial injector
Combust Flame, 249 (2023), Article 112595
View PDF View article View in Scopus ↗ Google Scholar ↗

[13] S. Marragou, H. Magnes, A. Aniello, L. Selle, T. Poinsot, T. Schuller
Experimental analysis and theoretical lift-off criterion for H_2 /air flames stabilized on a dual swirl injector
Proc Combust Inst, 39 (4) (2023), pp. 4345-4354
View PDF View article View in Scopus ↗ Google Scholar ↗

[14] T.G. Reichel, K. Goeckeler, O. Paschereit
Investigation of lean premixed swirl-stabilized hydrogen burner with axial air injection using OH-PLIF imaging
J Eng Gas Turbines Power, 137 (11) (2015), Article 111513
View in Scopus ↗ Google Scholar ↗

[15] T.G. Reichel, S. Terhaar, O. Paschereit
Increasing flashback resistance in lean premixed swirl-stabilized hydrogen combustion by axial air injection
J Eng Gas Turbines Power, 137 (7) (2015), Article 071503
View in Scopus ↗ Google Scholar ↗

[16] T.G. Reichel, C.O. Paschereit
Interaction mechanisms of fuel momentum with flashback limits in lean-premixed combustion of hydrogen
Int J Hydrog Energy, 42 (7) (2017), pp. 4518-4529
View PDF View article View in Scopus ↗ Google Scholar ↗

[17] E. Æsøy, J.G. Aguilar, S. Wiseman, M.R. Bothien, N.A. Worth, J.R. Dawson
Scaling and prediction of transfer functions in lean premixed H_2/CH_4-flames
Combust Flame, 215 (2020), pp. 269-282
View PDF View article View in Scopus ↗ Google Scholar ↗

[18] D. Mira, O. Lehmkuhl, A. Both, P. Stathopoulos, T. Tanneberger, T.G. Reichel, C.O. Paschereit, M. Vázquez, G. Houzeaux
Numerical characterization of a premixed hydrogen flame under conditions close to flashback
Flow Turbul Combust, 104 (2) (2020), pp. 479-507
Crossref ↗ View in Scopus ↗ Google Scholar ↗

[19] M. Vázquez, G. Houzeaux, S. Koric, A. Artigues, J. Aguado-Sierra, R. Arís, D. Mira, H. Calmet, F. Cucchietti, H. Owen, A. Taha, E.D. Burness, J.M. Cela, M. Valero
Alya: Multiphysics engineering simulation toward exascale
J Comput Sci, 14 (2016), pp. 15-27
View PDF View article View in Scopus ↗ Google Scholar ↗

[20] T. Capurso, D. Laera, E. Riber, B. Cuenot
NOx pathways in lean partially premixed swirling H_2-air turbulent flame
Combust Flame, 248 (2023), Article 112581
View PDF View article View in Scopus ↗ Google Scholar ↗

[21] AVBP
AVBP website:
(2002)
https://cerfacs.fr/avbp7x/index.php ↗
Google Scholar ↗

[22] J.-P. Legier, T. Poinsot, D. Veynante
Dynamically thickened flame LES model for premixed and non-premixed turbulent combustion
Proceedings of the summer program, vol. 12, Citeseer, Stanford University, Center for Turbulence Research (2000) (2000), pp. 157-168
View in Scopus ↗ Google Scholar ↗

[23] T.S. Cheng, C.Y. Wu, C.P. Chen, Y.H. Li, Y.C. Chao, T. Yuan, T.S. Leu
Detailed measurement and assessment of laminar hydrogen jet diffusion flames
Combust Flame, 146 (1) (2006), pp. 268-282
View PDF View article View in Scopus ↗ Google Scholar ↗

[24] H. Kahila, O. Kaario, Z. Ahmad, M. Ghaderi Masouleh, B. Tekgül, M. Larmi, V. Vuorinen
A large-eddy simulation study on the influence of diesel pilot spray quantity on methane-air flame initiation
Combust Flame, 206 (2019), pp. 506-521
View PDF View article View in Scopus ↗ Google Scholar ↗

[25] H. Kahila
Numerical modeling of spray-assisted dual-fuel ignition
[PhD thesis]
Aalto University (2019)
Google Scholar ↗

[26] B. Tekgül, P. Peltonen, H. Kahila, O. Kaario, V. Vuorinen
DLBFoam: An open-source dynamic load balancing model for fast reacting flow simulations in OpenFOAM
Comput Phys Comm, 267 (2021), Article 108073
View PDF View article View in Scopus ↗ Google Scholar ↗

[27] I. Morev, B. Tekgül, M. Gadalla, A. Shahanaghi, J. Kannan, S. Karimkashi, O. Kaario, V. Vuorinen
Fast reactive flow simulations using analytical Jacobian and dynamic load balancing in OpenFOAM
Phys Fluids, 34 (2) (2022), Article 021801
View in Scopus ↗ Google Scholar ↗

[28] J. Sun, Y. Wang, B. Tian, Z. Chen
detonationFoam: An open-source solver for simulation of gaseous detonation based on OpenFOAM
Comput Phys Comm, 292 (2023), Article 108859
View PDF View article View in Scopus ↗ Google Scholar ↗

[29] R. Mao, M. Lin, Y. Zhang, T. Zhang, Z.-Q.J. Xu, Z.X. Chen
DeepFlame: A deep learning empowered open-source platform for reacting flow simulations
Comput Phys Comm, 291 (2023), Article 108842
View PDF View article View in Scopus ↗ Google Scholar ↗

[30] A. Shahanaghi, S. Karimkashi, O. Kaario, V. Vuorinen
Efficient two-dimensional simulation of primary reference fuel ignition under engine-relevant thermal stratification
Phys Fluids, 35 (12) (2023), Article 126102
View in Scopus ↗ Google Scholar ↗

[31] J. Kannan, M. Gadalla, B. Tekgül, S. Karimkashi, O. Kaario, V. Vuorinen
Large-eddy simulation of tri-fuel ignition: diesel spray-assisted ignition of lean hydrogen–methane–air mixtures
Combust Theory Model, 25 (3) (2021), pp. 436-459
Crossref ↗ View in Scopus ↗ Google Scholar ↗

[32] P. Tamadonfar, S. Karimkashi, O. Kaario, V. Vuorinen
Inner flame front structures and burning velocities of premixed turbulent planar ammonia/air and methane/air flames
Flow Turbul Combust, 109 (2) (2022), pp. 477-513
Crossref ↗ View in Scopus ↗ Google Scholar ↗

[33] P. Tamadonfar, S. Karimkashi, O. Kaario, V. Vuorinen
A study of flame dynamics and structure in premixed turbulent planar NH_3/H_2/air flames
Int J Engine Res (2023), pp. 262-275
Google Scholar ↗

[34] S. Karimkashi, M. Gadalla, J. Kannan, B. Tekgül, O. Kaario, V. Vuorinen
Large-eddy simulation of diesel pilot spray ignition in lean methane-air and methanol-air mixtures at different ambient temperatures
Int J Engine Res, 24 (3) (2023), pp. 965-981
Crossref ↗ View in Scopus ↗ Google Scholar ↗

[35] S. Karimkashi, P. Tamadonfar, O. Kaario, V. Vuorinen
A numerical investigation on effects of hydrogen enrichment and turbulence on NO formation pathways in premixed ammonia/air flames
Combust Sci Technol (2023), pp. 1-30
Google Scholar ↗

[36] F. Weijie
Characteristics of ethylene–air continuous rotating detonation in the cavity-based annular combustor
Phys Fluids, 35 (4) (2023), Article 045142
Google Scholar ↗

[37] S. Hoffmann, R. Koch, H.-J. Bauer
Reacting flow prediction of the low-swirl lifted flame in an aeronautical combustor with angular air supply
Volume 3B: Combustion, fuels, and emissions, American Society of Mechanical Engineers, Boston, Massachusetts, USA (2023), Article V03BT04A041
Google Scholar ↗

[38] M. Gadalla, S. Karimkashi, I. Kabil, O. Kaario, T. Lu, V. Vuorinen
Embedded direct numerical simulation of ignition kernel evolution and flame initiation in dual-fuel spray assisted combustion
Combust Flame, 259 (2024), Article 113172

View PDF View article View in Scopus ↗ Google Scholar ↗

[39] CFD_ACE. CFD_ACE+ website: https://www.appliedmaterials.com/us/en/semiconductor/solutions-and-software/software-solutions/ace-plus-suite.html ↗.

Google Scholar ↗

[40] A. Dasgupta, E. Gonzalez-Juez, D.C. Haworth

Flame simulations with an open-source code

Comput Phys Comm, 237 (2019), pp. 219-229

View PDF View article View in Scopus ↗ Google Scholar ↗

[41] S. Zhong, F. Zhang, M. Jangi, X.-S. Bai, M. Yao, Z. Peng

Structure and propagation of n-heptane/air premixed flame in low temperature ignition regime

Appl Energy, 275 (2020), Article 115320

View PDF View article View in Scopus ↗ Google Scholar ↗

[42] N. Zhang, F. Zhang, S. Zhong, Z. Peng, J. Yu, H. Liu, C. Xu

Numerical and theoretical investigation of ethanol/air flame instability

Combust Theory Model, 24 (6) (2020), pp. 1108-1129

Crossref ↗ View in Scopus ↗ Google Scholar ↗

[43] S. Zhong, F. Zhang, Z. Peng, F. Bai, Q. Du

Roles of CO2 and H2O in premixed turbulent oxy-fuel combustion

Fuel, 234 (2018), pp. 1044-1054

View PDF View article View in Scopus ↗ Google Scholar ↗

[44] S. Zhong, F. Zhang, Q. Du, Z. Peng

Characteristics of reactivity controlled combustion with n-heptane low temperature reforming products

Fuel, 275 (2020), Article 117980

View PDF View article View in Scopus ↗ Google Scholar ↗

[45] R.C. Rocha, S. Zhong, L. Xu, X.-S. Bai, M. Costa, X. Cai, H. Kim, C. Brackmann, Z. Li, M. Aldén

Structure and laminar flame speed of an ammonia/methane/air premixed flame under varying pressure and equivalence ratio

Energy Fuels, 35 (9) (2021), pp. 7179-7192

Crossref ↗ View in Scopus ↗ Google Scholar ↗

[46] A. Rintanen, I. Morev

FickianTransportFoam:

(2024)

https://github.com/Aalto-CFD/FickianTransportFoam ↗

Google Scholar ↗

[47] A. Rintanen, A. Haider, Z. Shahin, I. Morev

DLBFoam hydrogen tutorials:

(2024)

https://github.com/Aalto-CFD/DLBFoam-Hydrogen-Tutorials ↗

Google Scholar ↗

[48] C. Greenshields

OpenFOAM v10 user guide

The OpenFOAM Foundation, London, UK (2022)
Google Scholar ↗

[49] C. Greenshields, H. Weller
Notes on computational fluid dynamics: General principles
CFD Direct Ltd (2022)
Google Scholar ↗

[50] K.E. Niemeyer, N.J. Curtis, C.-J. Sung
pyJac: Analytical Jacobian generator for chemical kinetics
Comput Phys Comm, 215 (2017), pp. 188-203
View PDF View article View in Scopus ↗ Google Scholar ↗

[51] E. Anderson, Z. Bai, C. Bischof, L.S. Blackford, J. Demmel, J. Dongarra, J. Du Croz, A. Greenbaum, S. Hammarling, A. McKenney, D. Sorensen
LAPACK users' guide
(3rd ed.), Society for Industrial and Applied Mathematics (1999)
Google Scholar ↗

[52] E. Hairer, G. Wanner
Solving ordinary differential equations II
Springer-Verlag, Berlin (1996)
Google Scholar ↗

[53] R. Tuominen
Coupling serpent and OpenFOAM for neutronics - CFD multi-physics calculations [Master's thesis]
Aalto university, Espoo, Helsinki (2015)
Google Scholar ↗

[54] R.J. Kee, M.E. Coltrin, P. Glarborg
Chemically reacting flow: Theory and practice
(1st ed.), Wiley (2003)
Google Scholar ↗

[55] C.F. Curtiss, J.O. Hirschfelder
Transport properties of multicomponent gas mixtures
J Chem Phys, 17 (6) (1949), pp. 550-555
Crossref ↗ View in Scopus ↗ Google Scholar ↗

[56] D. Goodwin, H. Moffat, I. Schoegl, R. Speth, R. Weber
Cantera: an abject-oriented software toolkit for chemical kinetics, thermodynamics, and transport processes
(2022)
https://www.cantera.org.Version2.6.0 ↗
Google Scholar ↗

[57] R. Palulli, S. Dybe, K. Zhang, F. Güthe, P.R. Alemela, C.O. Paschereit, C. Duwig
Characterisation of non-premixed, swirl-stabilised, wet hydrogen/air flame using large eddy simulation
Fuel, 350 (2023), Article 128710
View PDF View article View in Scopus ↗ Google Scholar ↗

[58] K. Zhang, Y. Shen, R. Palulli, A. Ghobadian, J. Nouri, C. Duwig
Combustion characteristics of steam-diluted decomposed ammonia in multiple-nozzle direct injection burner
Int J Hydrog Energy, 48 (42) (2023), pp. 16083-16099
View PDF View article View in Scopus ↗ Google Scholar ↗

[59] X. Wen, L. Berger, L. Cai, A. Parente, H. Pitsch
Thermodiffusively unstable laminar hydrogen flame in a sufficiently large 3D computational domain – Part I: Characteristic patterns
Combust Flame, 263 (2024), Article 113278
View PDF View article View in Scopus ↗ Google Scholar ↗

[60] H. Chu, L. Berger, M. Gauding, S. Pieper, H. Pitsch
Interactions of preferential diffusion and mixture inhomogeneities in hydrogen and iso-octane flame kernels under engine conditions
Combust Flame, 274 (2025), Article 113991
View PDF View article View in Scopus ↗ Google Scholar ↗

[61] F. Nicoud, F. Ducros
Subgrid-scale stress modelling based on the square of the velocity gradient tensor
Flow Turbul Combust, 62 (3) (1999), pp. 183-200
View in Scopus ↗ Google Scholar ↗

[62] P. Strempfl, O. Dounia, D. Laera, T. Poinsot
Effects of mixing assumptions and models for LES of hydrogen-fueled rotating detonation engines
Int J Hydrog Energy, 62 (2024), pp. 1-16
View PDF View article View in Scopus ↗ Google Scholar ↗

[63] S. Dillon, R. Mercier, B. Fiorina
Controlling the resolved flame thickness of non-premixed flames in LES with filtered tabulated chemistry
Proc Combust Inst, 40 (1) (2024), Article 105294
View PDF View article View in Scopus ↗ Google Scholar ↗

[64] V.I. Golovitchev, N. Nordin, R. Jarnicki, J. Chomiak
3-D diesel spray simulations using a new detailed chemistry turbulent combustion model
SAE Trans (2000), pp. 1391-1405
Google Scholar ↗

[65] S.B. Pope
Turbulent flows
(2000)
Google Scholar ↗

[66] S. Marragou, H. Magnes, T. Poinsot, L. Selle, T. Schuller
Stabilization regimes and pollutant emissions from a dual fuel CH_4/H_2 and dual swirl low NOx burner
Int J Hydrog Energy, 47 (44) (2022), pp. 19275-19288
View PDF View article View in Scopus ↗ Google Scholar ↗

[67] S.B. Pope

Ten questions concerning the large-eddy simulation of turbulent flows
New J Phys, 6 (1) (2004), p. 35
Google Scholar ↗

[68] I.B. Celik, Z.N. Cehreli, I. Yavuz
Index of resolution quality for large eddy simulations
J Fluids Eng, 127 (5) (2005), pp. 949-958
Crossref ↗ View in Scopus ↗ Google Scholar ↗

[69] L. Fangqing
A thorough description of how wall functions are implemented in OpenFOAM: Tech. rep.
Chalmers University of Technology, Sweden (2017)
Google Scholar ↗

[70] G. Vignat, D. Durox, S. Candel
The suitability of different swirl number definitions for describing swirl flows: Accurate, common and (over-) simplified formulations
Prog Energy Combust Sci, 89 (2022), Article 100969
View PDF View article View in Scopus ↗ Google Scholar ↗

[71] M. Matalon, B.J. Matkowsky
Flames as gasdynamic discontinuities
J Fluid Mech, 124 (1982), pp. 239-259
View in Scopus ↗ Google Scholar ↗

[72] A.J. Aspden, M.S. Day, J.B. Bell
Characterization of low Lewis number flames
Proc Combust Inst, 33 (1) (2011), pp. 1463-1471
View PDF View article View in Scopus ↗ Google Scholar ↗

[73] A.J. Aspden, M.S. Day, J.B. Bell
Lewis number effects in distributed flames
Proc Combust Inst, 33 (1) (2011), pp. 1473-1480
View PDF View article View in Scopus ↗ Google Scholar ↗

[74] N. Burali, S. Lapointe, B. Bobbitt, G. Blanquart, Y. Xuan
Assessment of the constant non-unity Lewis number assumption in chemically-reacting flows
Combust Theory Model, 20 (4) (2016), pp. 632-657
Crossref ↗ View in Scopus ↗ Google Scholar ↗

[75] C. Altantzis, C.E. Frouzakis, A.G. Tomboulides, S.G. Kerkemeier, K. Boulouchos
Detailed numerical simulations of intrinsically unstable two-dimensional planar lean premixed hydrogen/air flames
Proc Combust Inst, 33 (1) (2011), pp. 1261-1268
View PDF View article View in Scopus ↗ Google Scholar ↗

[76] R.W. Bilger
The structure of turbulent nonpremixed flames
Symp (Int) Combust, 22 (1) (1989), pp. 475-488
View PDF View article View in Scopus ↗ Google Scholar ↗

[77] Mahti supercomputer specifications

(2024)
https://docs.csc.fi/computing/systems-mahti/ ↗
Google Scholar ↗

Cited by (0)

1 A. Haider, I. Morev, A. Rintanen, and Z. Shahin have all made equal contribution to the results.

Published by Elsevier Ltd on behalf of Hydrogen Energy Publications LLC.